



Cite this: *J. Mater. Chem. A*, 2021, 9, 19179

# Biomimetic photocatalysts for the conversion of aqueous- and gas-phase nitrogen species to molecular nitrogen *via* denitrification and ammonia oxidation

Cheolwoo Park,<sup>†ab</sup> Hyelim Kwak,<sup>†a</sup> Gun-hee Moon<sup>ID</sup>\*<sup>c</sup> and Wooyul Kim<sup>ID</sup>\*<sup>a</sup>

Denitrification and anaerobic ammonium oxidation (anammox) are important biological processes of the nitrogen cycle that help to preserve the global ecosystem. However, indiscriminate development and global population growth result in the discharge of large amounts of nitrogen species (e.g., *via* the Haber–Bosch process), particularly nitrogen oxides and ammonia, which cannot be fully digested by microorganisms and therefore accumulate in soil and water. Photocatalysts can promote the conversion of nitrogen oxides and ammonia to molecular nitrogen under the action of photogenerated electrons and holes, thus mimicking denitrifying and anammox bacteria, respectively. Herein, we review the biomimetic photocatalysts and photoelectrochemical cells used to convert aqueous and airborne nitrogen species to molecular nitrogen and shed light on the charge transfer mechanism that should be selectively controlled to favor the formation of molecular nitrogen over that of nitrogen-containing intermediates and by-products. Last but not least, we discuss the outlooks and perspectives of solar-powered molecular nitrogen recovery and suggest guidelines for the design of high-performance denitrification/anammox bacteria-like photocatalysts.

Received 30th March 2021  
Accepted 30th June 2021

DOI: 10.1039/d1ta02644e

rsc.li/materials-a

<sup>a</sup>Department of Chemical and Biological Engineering, Research Institute of Global Environment, Sookmyung Women's University, 99, Cheongpa-ro 47-gil, Yongsan-gu, Seoul 04310, Republic of Korea. E-mail: wkim@sookmyung.ac.kr

<sup>b</sup>Department of Energy Science, Sungkyunkwan University, 2066, Seobu-ro, Jangan-Gu, Suwon, Gyeonggi-do 16419, Republic of Korea

<sup>c</sup>Extreme Materials Research Center, Korea Institute of Science and Technology (KIST), 5, Hwarang-ro 14-gil, Seongbuk-gu, Seoul 02792, Republic of Korea. E-mail: catalysis@kist.re.kr

<sup>†</sup> These authors contributed equally.

## 1. Introduction

Unlike ammonia (NH<sub>3</sub>), nitrite (NO<sub>2</sub><sup>-</sup>), and nitrate (NO<sub>3</sub><sup>-</sup>), molecular nitrogen (N<sub>2</sub>), which constitutes ~80% of the atmosphere by volume, is not chemically and biologically reactive and cannot therefore be utilized by plants for the synthesis of proteins to be supplied to animals and humans.<sup>1,2</sup> The conversion of N<sub>2</sub> into more reactive forms mainly occurs through microbially facilitated processes such as nitrogen fixation and



Cheolwoo Park received a BS in Biochemical Engineering from Gangneung-Wonju National University in 2015 and is now pursuing a PhD in Energy Science under the supervision of Prof. Tae Kyu Ahn at Sungkyunkwan University (SKKU). He joined Sookmyung Women's University (advisor: Prof. Wooyul Kim) as a visiting researcher in 2016 and focuses

on elucidating the reaction mechanisms of surface-modified metal oxide photocatalysts for energy conversion and environmental applications.



Hyelim Kwak received a BS in Chemical and Biological Engineering from Sookmyung Women's University (Seoul, Korea) in 2020 and is currently pursuing a master's degree under the supervision of Prof. Wooyul Kim at Sookmyung Women's University, focusing on photocatalysis for environmental and energy applications.

nitrification. The fixed reactive forms are absorbed, used, released in the form of excrements and dead bodies, converted back to the biologically inert form (*i.e.*, N<sub>2</sub>) through denitrification and anammox, and eventually returned to the atmosphere.<sup>1</sup> This biological nitrogen cycle preserved the balance between nitrogen fixation and denitrification for thousands of years.<sup>2</sup> In the 20<sup>th</sup> century, however, human activities began to strongly impact the modern nitrogen cycle (established some 2.5 billion years ago), which is likely to result in the establishment of a new steady state in several decades.

Over the past century, the development of industrial processes and the rapid increase in fossil fuel use to satisfy the growing global demand for food and energy have drastically disrupted the nitrogen cycle.<sup>3–9</sup> In particular, the Haber–Bosch process offers a way to synthetically fix nitrogen in the form of ammonia for the mass production of synthetic fertilizers,<sup>3</sup> thus enabling abundant food production along with rapid world population growth. In the last 50 years, the consumption of fertilizers and fossil fuels has increased more than six-fold<sup>4,5</sup> and three-fold,<sup>6</sup> respectively. The projected global population growth is expected to result in elevated fertilizer production and fossil fuel consumption. As both of these anthropogenic sources (*i.e.*, the Haber–Bosch process and fossil fuel combustion) account for ~45% of the annual fixed nitrogen production (Fig. 1a), the above increase will initiate a cascade of large-scale environmental impacts such as (i) the extensive eutrophication of terrestrial and aquatic systems, (ii) the increase in potent greenhouse gas (*i.e.*, N<sub>2</sub>O) inventory, and (iii) global acidification. The low (typically <40%) utilization efficiency of the nitrogen contained in fertilizers results in the nitrification-

based conversion of large amounts of fertilizer (~90% of NH<sub>4</sub><sup>+</sup>) to highly mobile NO<sub>3</sub><sup>-</sup> ions, which can leach into aquatic systems such as rivers, lakes, and aquifers.<sup>2</sup> Moreover, besides producing N<sub>2</sub> as the main product, anaerobic denitrification also affords N<sub>2</sub>O and thus significantly affects atmospheric N<sub>2</sub>O levels.<sup>7</sup> As N<sub>2</sub>O reacts with the stratospheric ozone and is a potent greenhouse gas with global warming potential ~300 times that of CO<sub>2</sub>, denitrification contributes to climate change and stratospheric ozone depletion.<sup>7</sup> In addition, the absorption of nitrogen compounds by agricultural soils results in their acidification and thus inhibits the activity of soil organisms and disturbs the ecosystem. Fertilizer nitrogen is easily converted into gaseous ammonia and therefore returns from the atmosphere to the watershed *via* precipitation as another reactive nitrogen form.<sup>8</sup> Nitrogen oxides (NO<sub>x</sub>) produced by fossil fuel combustion not only react with ammonia to produce fine dust and ozone and thus contribute to poor air quality, but also cause acid rain and, hence, soil and ocean acidification. The nitrogen cycle, the carbon cycle, and climate are known to exhibit numerous strong mutual interactions.<sup>9</sup> The dramatic increase in atmospheric CO<sub>2</sub> levels (>30% above pre-industrial values) due to fossil fuel combustion and land use change is viewed as the primary cause of climate warming observed over the past century. The human activity-induced perturbations of global nitrogen and carbon cycles are in part related to each other, as exemplified by the possible interacting drivers of these cycles during the 21<sup>st</sup> century (Fig. 1b).

From the perspective of nitrogen cycle management, the main objectives requiring special consideration are (i) the substantial decrease in nitrogen use,<sup>9</sup> (ii) the direct up-cycling of



*Gun-hee Moon received a BS in Chemical Engineering from Inha University (Incheon, Korea) in 2008, an MS degree in Environmental Engineering from POSTECH in 2011, and a PhD degree in Chemical Engineering from POSTECH (Pohang, Korea) in 2015. After a postdoctoral stay at the Max-Planck-Institut für Kohlenforschung (Germany, 2016–2020), he moved to the Korea Institute of Science and*

*Technology (KIST), where he is currently employed as a senior scientist working on the design of photocatalysts, electrocatalysts, photoelectrochemical cells, and carbon materials for energy conversion and environmental applications.*



*Wooyul Kim received a PhD in Environmental Engineering (advisor: Prof. Wonyong Choi) from POSTECH (Pohang, Korea) in 2012 and worked at the Lawrence Berkeley National Laboratory (USA, 2012–2016) as a postdoctoral fellow (advisor: Dr Heinz Frei). During his PhD period, he joined Osaka University (advisor: Prof. Tetsuro Majima) as a visiting researcher in 2009, 2010, and 2012. He*

*joined the faculty of the Department of Chemical and Biological Engineering at Sookmyung Women's University (Seoul, Korea) as an assistant professor (2016) and was promoted to associate professor in 2021. His current research focuses on revealing the structural identity of key intermediates and their roles in the catalytic cycle (*i.e.*, their kinetic relevancy) to overcome the kinetic barriers for photo (or electro) catalysis. At an early stage of his independent career within the fields of photo(electro) catalysis for energy and environmental applications, he was honored as a winner of the 2020 Energy & Environmental Science lectureship award (Royal Society of Chemistry).*



Fig. 1 (a) Rates of nitrogen flux in the modern nitrogen cycle depend on the efficiency of transformations between reservoirs. Reprinted with permission from ref. 2. Copyright© 2010, American Association for the Advancement of Science. (b) The main anthropogenic drivers of nitrogen-carbon-climate interactions in the 21<sup>st</sup> century. Reprinted with permission from ref. 9. Copyright© 2008, Nature Publishing Group.

used nitrogen to microbial protein,<sup>10</sup> and (iii) the development of artificial denitrification processes powered by renewable energy. Among the various methods of decreasing nitrogen use, one can mention systematic crop rotation,<sup>10</sup> optimization of fertilizer introduction timing and amount,<sup>11</sup> and the breeding/development of genetically engineered crops for increasing nitrogen use efficiency.<sup>12</sup> In view of the low efficiency of nitrogen utilization (*e.g.*, agricultural nitrogen utilization efficiency = 40%, feed conversion efficiency = 15%, manure utilization efficiency = 50%),<sup>10</sup> the direct up-cycling of used nitrogen to microbial protein has been proposed as an alternative to the formation of plant and meat proteins. As a renewable energy-powered direct denitrification process, the photocatalytic reduction of reactive nitrogen compounds to N<sub>2</sub> holds great promise since the advantages of photocatalysis compared with conventional catalysis, thermocatalysis, and electrocatalysis are that (i) it does not require energy-intensive processes (solar energy *vs.* heat or electricity), (ii) the operation is possible

without the need for oxidants, reductants, or electrolytes, (iii) it is flexible for application in both aqueous and gas-phase reactions, and (iv) material cost is relatively cheap.<sup>13–17</sup> Herein, we introduce and discuss the most recent findings and advances in photocatalytic denitrification and ammonia oxidation processes, the ultimate goal of which is the conversion of reactive nitrogen compounds (*e.g.*, ionic or gas-phase nitrogen oxides, ammonia) into inert N<sub>2</sub> on a scale comparable to that of anthropogenic nitrogen fixation. Most parts of this review deal with denitrification/anammox bacteria-like photocatalysts and the related mechanisms, which greatly affect activity and selectivity.

## 2. Photocatalysts and co-catalysts for denitrification

### 2.1. Reduction of ionic nitrogen oxides to N<sub>2</sub>

The nitrogen cycle imbalance due to human activities (*e.g.*, combustion, intensive fertilizer use, and agriculture) has resulted in increased nitrate levels in groundwater and other waters. Ionic nitrogen oxides including nitrate, nitrite, and NO<sup>-</sup> are the prevalent contaminants in groundwater, causing eutrophication, water waste, and potentially health-threatening consequences such as cancer, birth defects, and cyanosis. Therefore, the release of ionic nitrogen oxides is strictly regulated, and their removal to secure water resources is a great challenge. Traditionally, the removal of NO<sub>3</sub><sup>-</sup> from wastewater is achieved using reverse osmosis, ion exchange, and biological/catalytic treatment.<sup>1,18,19</sup>

Among the various denitrification methods used to reduce ionic nitrogen oxides in aquatic environments, eco-friendly photocatalytic denitrification is the one most promising from the perspective of industrialization.<sup>20–22</sup> This photocatalytic reduction affords inert N<sub>2</sub> gas and mainly involves the reduction of NO<sub>3</sub><sup>-</sup> to N<sub>2</sub> *via* NO<sub>2</sub><sup>-</sup>.<sup>20,23–27</sup> To increase the overall efficiency and selectivity for N<sub>2</sub> formation, one needs to fully understand the underlying mechanisms, including those of the undesired nitrification (conversion of NO<sub>2</sub><sup>-</sup> to NO<sub>3</sub><sup>-</sup>)<sup>28,29</sup> and the dissimilatory nitrate reduction to ammonium (DNRA).<sup>30,31</sup> In particular, these undesired reactions need to be precisely controlled (*i.e.*, inhibited) to maximize N<sub>2</sub> formation selectivity. However, from the perspective of reactive nitrogen up-cycling, the highly selective production of ammonium (*e.g.*, DNRA) could be useful.<sup>32,33</sup> In this section, we critically investigate the efforts made to enhance the selectivity for N<sub>2</sub> production in the photocatalytic denitrification of ionic nitrogen oxides and the efficiency of this process. In particular, we demonstrate the important roles of intrinsic photocatalyst properties, sacrificial agents, and specific reaction conditions.

**2.1.1. Photocatalytic materials for ionic nitrogen oxide reduction to N<sub>2</sub>.** The discovery of the photocatalytic reduction of NO<sub>3</sub><sup>-</sup> to NH<sub>4</sub><sup>+</sup> in aqueous solutions (over Pt–TiO<sub>2</sub>) in 1987<sup>34</sup> triggered the search for other denitrification photocatalysts. In nature, the corresponding reaction involves multiple-electron transfer and is primarily performed by bacteria such as *Thiobacillus denitrificans* ( $2\text{NO}_3^- + 10\text{e}^- + 12\text{H}^+ \rightarrow \text{N}_2 + 6\text{H}_2\text{O}$ ),

whereas photocatalytic denitrification predominantly occurs in a stepwise manner and involves the reduction of  $\text{NO}_3^-$  to  $\text{NO}_2^-$  and the subsequent reduction of  $\text{NO}_2^-$  to  $\text{N}_2$  or  $\text{NH}_4^+$ .<sup>20,35–38</sup> Each step of the nitrate-to- $\text{N}_2$  reduction has its own rate constant, which is largely determined by the interaction between the photocatalyst and the adsorbed reactants (e.g.,  $\text{NO}_3^-$ ,  $\text{NO}_2^-$ ,  $\text{NO}$ , and  $\text{N}_2\text{O}$ ) and reflects the ease of reactant adsorption on or product desorption from the photocatalyst.<sup>39</sup> Attempts to accelerate photocatalytic denitrification have resulted in the discovery and evaluation of numerous photocatalysts, among which  $\text{TiO}_2$  is the one most frequently and thoroughly studied because of its durability, non-toxicity, long diffusion length of charge carriers, and other advantages. In particular, various methods of photocatalyst surface modification have been developed to accelerate photoconversion or alter the reaction mechanism and thus control selectivity. According to surface modifier type, these methods are classified into those relying on metal deposition,<sup>40,41</sup> inorganic adsorbates,<sup>42,43</sup> polymer coatings, dye sensitization,<sup>44–47</sup> impurity doping, charge transfer complexation,<sup>48,49</sup> etc. Photocatalyst modification not only increases photoconversion efficiency but also affects selectivity by influencing the mechanism and kinetics of photocatalytic denitrification. Recent studies on photocatalysis by surface-modified semiconductors are summarized below.

*Photocatalysts based on pristine  $\text{TiO}_2$  and related (bi)metallic composites.* Compared to  $\text{TiO}_2$  powder (P25),  $\text{TiO}_2$  nanotubes (TNTs) achieved a ~50% higher  $\text{NO}_3^-$  conversion efficiency and a slightly elevated selectivity for  $\text{N}_2$  formation, which was ascribed to their high specific surface area and abundant active sites.<sup>21</sup> Given that bare  $\text{TiO}_2$  exhibits poor selectivity for  $\text{N}_2$  formation,  $\text{TiO}_2$ -metal composites ( $\text{M}/\text{TiO}_2$ ) have been used for  $\text{NO}_3^-$  reduction in aquatic environments. The deposited metal changes the reactant adsorption properties and the charge carrier dynamics under illumination by modifying surface properties such as the space-charge region and charge density. In particular, metals deposited on  $\text{TiO}_2$  promote its use as an electron sink (with the formation of a Schottky barrier potential) by decreasing the work function and, hence, increasing the electron affinity.<sup>20</sup> Sá *et al.* reported that the deposition of Cu, Fe, and Ag on  $\text{TiO}_2$  increased its activity and selectivity for  $\text{N}_2$ , suggesting that the conversion efficiency and selectivity strongly depend on factors such as reaction temperature, hole scavenger presence/type, metal deposition method, and  $\text{TiO}_2$  particle size. Among the various  $\text{M}/\text{TiO}_2$  composites,  $\text{Ag}/\text{TiO}_2$  showed the highest activity to meet the EU-stipulated levels for drinking water (Table 1).<sup>50</sup> The surface plasmon resonance effect of  $\text{Ag}^0$  and  $\text{Au}^0$  on  $\text{TiO}_2$  extended the excitation range of this oxide semiconductor from UV to visible and promoted the separation of photogenerated charge carriers (Fig. 2a).<sup>51</sup> Compared to other  $\text{M}/\text{TiO}_2$  composites,  $\text{Ag}/\text{TiO}_2$  exhibited high selectivity for the reduction of  $\text{NO}_3^-$  to  $\text{N}_2$ ,<sup>21,40,41</sup> while  $\text{Au}/\text{TiO}_2$  accelerated the formation of  $\text{NH}_4^+$ .<sup>51</sup> The non-noble metals/ $\text{TiO}_2$  (Cu, Ni, Fe, Bi, Zn, etc.) composites also exhibited enhanced catalytic performance.<sup>33,52–54</sup> For instance,  $\text{Fe}/\text{TiO}_2$  and  $\text{Zn}/\text{TiO}_2$  exhibited better  $\text{N}_2$  yield and selectivity than bare  $\text{TiO}_2$ .<sup>54–56</sup> Regarding  $\text{Cu}/\text{TiO}_2$  and  $\text{Ni}/\text{TiO}_2$ , the formation of  $\text{NO}_2^-$  and  $\text{NH}_4^+$  was predominant, where the nitrate reduction was facilitated by the

electrons accumulated on Cu or Ni but the interaction with intermediates inhibited the generation of  $\text{N}_2$ .<sup>33,50,54</sup> On the other hand,  $\text{Cr}/\text{TiO}_2$  and  $\text{Co}/\text{TiO}_2$  lowered the conversion of  $\text{NO}_3^-$ , which was explained by the light shield effect at a specific wavelength and the fast charge recombination kinetics as well.<sup>33,54</sup> However, conventional metal-modified photocatalysts usually suffer from metal leaching, aggregation, and gradual deactivation and need to be substantially optimized in terms of  $\text{N}_2$  formation selectivity.

In bimetallic composites, the metals act as promoters and selectors. The promoter metal (e.g., Cu, Sn, In)<sup>57–59</sup> initiates the rate-limiting step of the  $\text{NO}_3^-$  to  $\text{NO}_2^-$  conversion, while the selector metal (e.g., Pd, Pt, Rh)<sup>60,61</sup> further reduces  $\text{NO}_2^-$  to  $\text{NH}_4^+$  and/or  $\text{N}_2$ . Among the available metal combinations, Pd-Cu is widely accepted as the most active and selective one for electrocatalytic  $\text{NO}_3^-$  reduction, the mechanism of which has been revealed by conventional electrochemical analysis and density functional theory (DFT) calculations.<sup>45,46</sup> The increased  $\text{H}_2$  amount resulting from the elevated Pd loading and  $\text{H}_2$  flow rate promoted the reduction of  $\text{Cu}^{\text{II}}$  to  $\text{Cu}^0$  and thus facilitated  $\text{NO}_3^-$  removal, while the high N:H ratio on the active Pd sites increased the selectivity for  $\text{N}_2$ .<sup>62</sup> Bimetallic electrocatalysts have been widely deposited on photocatalysts for photocatalytic applications.<sup>63</sup> Precious metal (e.g., Pt, Pd)-Cu combinations are among those offering the highest activity and selectivity for catalytic  $\text{NO}_3^-$  reduction (Table 1). Notably,  $\text{NO}_3^-$  was mainly converted to ammonia (over Pt/ $\text{TiO}_2$ ) or  $\text{NO}_2^-$  (over Cu/ $\text{TiO}_2$ ), whereas Pt-Cu/ $\text{TiO}_2$  catalysts exhibited a considerable selectivity for  $\text{N}_2$  formation in photocatalytic  $\text{NO}_3^-$  reduction.<sup>64</sup> The fact that  $\text{N}_2$  formation was observed for Pd/ $\text{TiO}_2$  and Pd-Cu/ $\text{TiO}_2$  systems but was negligible for the Cu- $\text{TiO}_2$  system means that Pd is indispensable for the photocatalytic reduction of  $\text{NO}_2^-$  to  $\text{N}_2$ .<sup>65,66</sup> Likewise, in bimetallic composites, electrons transferred from  $\text{TiO}_2$  to promoter metal sites reduce  $\text{NO}_3^-$  to  $\text{NO}_2^-$ , with the subsequent reduction of  $\text{NO}_2^-$  to  $\text{N}_2$  occurring at selector metal sites. The adsorption of protons on the selector metal surface significantly affects the overall selectivity for  $\text{N}_2$  (Fig. 2b). Hence, the metal deposited on  $\text{TiO}_2$  controls the reaction path and, hence, the conversion efficiency and selectivity for  $\text{N}_2$  or  $\text{NH}_4^+$ , which implies that the optimization of the promoter-to-selector metal ratio is crucial for realizing selective  $\text{N}_2$  formation. Finally, the presence of sacrificial electron donors and the occurrence of competitive reactions (e.g.,  $\text{H}_2$  production) present additional challenges.

*New photocatalyst types.* Much effort has been directed at the optimization of perovskite-based photocatalysts, as the unique properties of perovskites (e.g., chemical and optical stability, tunable bandgap and crystal structure, and long charge carrier lifetime) allow one to readily alter the dynamics of photo-generated charge carriers and the overall photocatalysis mechanism. Pd/GdCrO<sub>3</sub> exhibited faster nitrate reduction and higher selectivity for  $\text{N}_2$  due to the negative conduction band energy level and the co-catalyst effect of Pd,<sup>67</sup> while FeTiO<sub>3</sub> was characterized by negligible  $\text{NH}_4^+$  formation (i.e., it exhibited a remarkably high selectivity for  $\text{N}_2$ ) without the need for complex and expensive catalysts.<sup>68</sup> KTaO<sub>3</sub> effectively promoted the photocatalytic reduction of  $\text{NO}_3^-$  to  $\text{NO}_2^-$ ,  $\text{N}_2$ , and  $\text{NH}_3$

Table 1 Materials used for the photocatalytic reduction of ionic nitrogen oxides

No.	Photocatalyst	Co-catalyst	Light	Initial conc.	Catalyst loading (g L <sup>-1</sup> )	Sacrificial reagent	NO <sub>3</sub> <sup>-</sup> conversion (%)	N <sub>2</sub> selectivity (%)	By-products	Ref.
1	TiO <sub>2</sub>	—	Medium-pressure Hg lamp, 150 W	1 mM	2.5	Oxalic acid	15	—	NH <sub>4</sub> <sup>+</sup>	82
2	TiO <sub>2</sub>	—	Medium-pressure Hg lamp, 400 W	10 mM	10	Oxalic acid	9.8	56.5	NO <sub>2</sub> <sup>-</sup> , NH <sub>4</sub> <sup>+</sup>	33
3	TiO <sub>2</sub>	—	Medium-pressure Hg lamp, 150 W	0.8 mM	0.45	Oxalic acid	90.1	55.4	NO <sub>2</sub> <sup>-</sup> , NH <sub>4</sub> <sup>+</sup>	68
4	TiO <sub>2</sub>	—	High-pressure Hg lamp, 100 W	0.8 mM	0.38	Formic acid	48.5	38.1	NO <sub>2</sub> <sup>-</sup> , NH <sub>4</sub> <sup>+</sup>	80
5						KI	25.5	18		
6	TiO <sub>2</sub>	—	High-pressure Hg lamp, 300 W	1.6 mM	1	Formic acid	26.8	72.4	NO <sub>2</sub> <sup>-</sup> , NH <sub>4</sub> <sup>+</sup>	81
7	TiO <sub>2</sub>	—	High-pressure Hg lamp, 150 W	1.6 mM	1	Formic acid	35.8	87.7	NO <sub>2</sub> <sup>-</sup> , NH <sub>4</sub> <sup>+</sup>	21
8	TiO <sub>2</sub> (TNTs)	—	400 W lamp	1.6 mM	0.21	Oxalic acid	53.3	89.5	NO <sub>2</sub> <sup>-</sup> , NH <sub>4</sub> <sup>+</sup>	
9	TiO <sub>2</sub>	Au	High-pressure Hg lamp, 100 ppm	1.6 mM	0.38	Formic acid	44	—	NH <sub>4</sub> <sup>+</sup>	83
10	TiO <sub>2</sub>	Cu	High-pressure Hg lamp, 110 W	100 ppm	0.38	Formic acid	100	63	NH <sub>4</sub> <sup>+</sup>	50
11	TiO <sub>2</sub>	Ag	High-pressure Hg lamp, 300 W	1.6 mM	1	Formic acid	99.6	88.4	NO <sub>2</sub> <sup>-</sup> , NH <sub>4</sub> <sup>+</sup>	81
12	TiO <sub>2</sub>	Ag <sub>2</sub> O	High-pressure Hg lamp, 150 W	1.6 mM	1	Formic acid	97.5	82.9	NO <sub>2</sub> <sup>-</sup> , NH <sub>4</sub> <sup>+</sup>	
13	TiO <sub>2</sub> (TNTs)	AgCl	High-pressure Hg lamp, 150 W	1.6 mM	1	Formic acid	94.5	92.9	NO <sub>2</sub> <sup>-</sup> , NH <sub>4</sub> <sup>+</sup>	21
14	TiO <sub>2</sub>	Pt–Cu	High-pressure Hg lamp, 250 W	60 mg L <sup>-1</sup>	1	Benzene	59	~89	NO <sub>2</sub> <sup>-</sup> , NH <sub>4</sub> <sup>+</sup>	64
15	TiO <sub>2</sub>	Pd–Cu	High-pressure Hg lamp, 400 W	0.05 mM	100	Formic acid	56	98	NO <sub>2</sub> <sup>-</sup>	65
16	TiO <sub>2</sub>	Pd–Cu	Medium-pressure Hg lamp, 150 W	1.6 mM	0.52	Formic acid	84	83	NO <sub>2</sub> <sup>-</sup> , NH <sub>4</sub> <sup>+</sup>	66
17	LiNbO <sub>3</sub>	—	High-pressure Hg lamp, 100 W	0.8 mM	0.38	Formic acid	98.4	95.8	NO <sub>2</sub> <sup>-</sup> , NH <sub>4</sub> <sup>+</sup>	80
18		—	High-pressure Hg lamp, 100 W	0.8 mM	0.38	KI	96.2	93	NO <sub>2</sub> <sup>-</sup> , NH <sub>4</sub> <sup>+</sup>	
19	LiNbO <sub>3</sub>	—	UV lamp	10 mg L <sup>-1</sup>	Membrane	Formic acid	81.82	98.04	NO <sub>2</sub> <sup>-</sup> , NH <sub>4</sub> <sup>+</sup>	22
20	LiNbO <sub>3</sub>	—	High-pressure Hg lamp, 100 W	0.8 mM	0.4	Formic acid	60.5	57.21	NO <sub>2</sub> <sup>-</sup> , NH <sub>4</sub> <sup>+</sup>	76
21		Fe	High-pressure Hg lamp, 100 W	0.8 mM	0.4	Formic acid	86.69	85.71	NO <sub>2</sub> <sup>-</sup> , NH <sub>4</sub> <sup>+</sup>	
22	CuInS <sub>2</sub>	0.75 wt% Pt–0.75 wt% Ru	Hg lamp, 125 W	7.2 mg L <sup>-1</sup>	0.5	Sodium oxalate	100	80.2	NO <sub>2</sub> <sup>-</sup>	77
23			Xe lamp, 300 W (400 nm cut-off)	7.2 mg L <sup>-1</sup>	0.5	Sodium oxalate	100	56.1	NO <sub>2</sub> <sup>-</sup>	
24	FeTiO <sub>3</sub>	—	Medium-pressure Hg lamp, 150 W	0.8 mM	0.45	Oxalic acid	100	93	NO <sub>2</sub> <sup>-</sup>	68
25	GdCrO <sub>3</sub>	1 wt% Pd	High-pressure Hg lamp, 500 W	0.8 mM	0.5	Formic acid	98.7	100	—	67
26		1 wt% Ag	High-pressure Hg lamp, 500 W	0.8 mM	0.5	Formic acid	85.1	83.2	NO <sub>2</sub> <sup>-</sup> , NH <sub>4</sub> <sup>+</sup>	
27		1 wt% Cu	High-pressure Hg lamp, 500 W	0.8 mM	0.5	Formic acid	81.9	78.8	NO <sub>2</sub> <sup>-</sup> , NH <sub>4</sub> <sup>+</sup>	
28		—	High-pressure Hg lamp, 500 W	0.8 mM	0.5	Formic acid	79.3	81.4	NO <sub>2</sub> <sup>-</sup> , NH <sub>4</sub> <sup>+</sup>	
29	CuFe <sub>0.7</sub> Cr <sub>0.3</sub> S <sub>2</sub>	0.75 wt% Pd	Hg lamp, 500 W	1.6 mM	1	Sodium oxalate	100	59	NO <sub>2</sub> <sup>-</sup>	78
30	KTaO <sub>3</sub>	3 wt% Au	High-pressure Hg lamp, 450 W	10 mM	2.5	—	97	44	H <sub>2</sub> , NO <sub>2</sub> <sup>-</sup> , NH <sub>4</sub> <sup>+</sup>	69

under UV light irradiation even in the absence of co-catalysts or reducing reagents such as organic compounds.<sup>69</sup>

Layered double hydroxides (LDHs) with hydrotalcite-like structures are some of the interesting materials due to their unique properties such as anions intercalated in 2D interlayer spaces, a bunch of surface hydroxyl groups, flexibility to change elements, and swelling nature, where divalent (*e.g.*, Mg, Co, Ni, Cu, and Zn) and trivalent (*e.g.*, Al, Cr, Ni, and Ga) metal cations are combined.<sup>70,71</sup> In particular, a high specific surface area, excellent electrical conductivity, high mobility of charge carriers, and high chemical stability make it possible to apply

them in various photocatalytic reactions.<sup>72–74</sup> Therefore, it was reported that the MgAl-LDH used for NO<sub>3</sub><sup>-</sup> reduction enhanced the selectivity to N<sub>2</sub> without any sacrificial reagent, which was ascribed to both attraction of NO<sub>3</sub><sup>-</sup> ions near the photocatalyst surface and restriction of charge carrier recombination.<sup>75</sup>

LiNbO<sub>3</sub> is a nonlinear optical material with high potential for NO<sub>3</sub><sup>-</sup> removal,<sup>22,60,76</sup> offering spontaneous polarization screening by either free electrons and holes or ions/molecules adsorbed on the surface. The second harmonic generation effects of nonlinear optical materials facilitate the generation of electrons and inhibit the recombination of charge carriers to

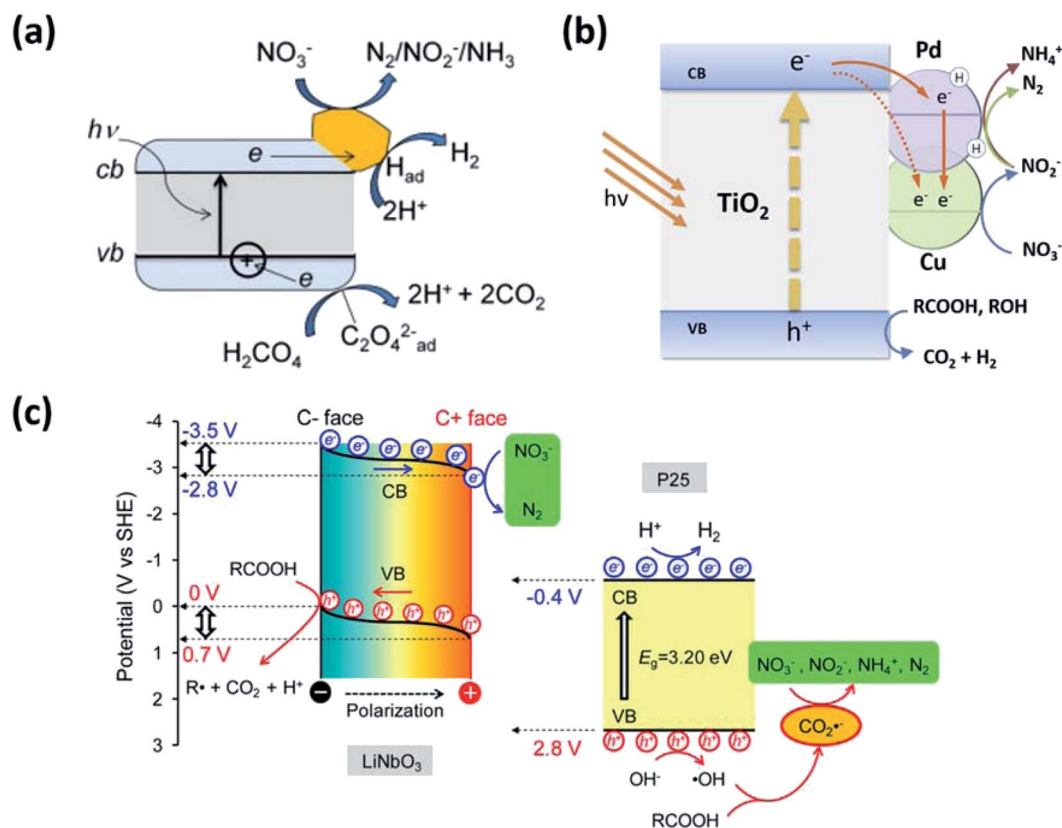


Fig. 2 Photocatalytic nitrate reduction promoted by (a) Au/TiO<sub>2</sub> and (b) Pd–Cu/TiO<sub>2</sub>. Reprinted with permission from ref. 51 and 66. Copyright© 2011 and 2014, Elsevier. (c) Comparison of nitrate reduction promoted by LiNbO<sub>3</sub> and P25 TiO<sub>2</sub>. Reprinted with permission from ref. 80. Copyright© 2016, American Chemical Society.

enhance the efficiency and stability of NO<sub>3</sub><sup>−</sup> reduction. The superior (compared to that of bare TiO<sub>2</sub>) activity of LiNbO<sub>3</sub> was attributed to the photocatalytic reduction of nitrate through direct heterogeneous interactions with electrons at the conduction band of this material, whereas in the conventional photocatalysis mechanism, nitrate is mainly reduced by CO<sub>2</sub><sup>•−</sup> generated from holes at the valence band (Fig. 2c). In an effort to develop a systematic and durable industrial-scale process, LiNbO<sub>3</sub> was applied to a membrane platform,<sup>22</sup> which offered the inherent benefits of high separation performance and antifouling properties compared to common ultrafiltration membranes. In addition, LiNbO<sub>3</sub> has been successfully applied to membrane materials without significant photocatalytic activity inhibition (Table 1). Fe–LiNbO<sub>3</sub> exhibited an enhanced selectivity for N<sub>2</sub> formation as well as a high NO<sub>3</sub><sup>−</sup> conversion efficiency,<sup>76</sup> which was ascribed to the increase in the specific surface area and the number of Lewis-acidic sites upon doping.

As wide-bandgap semiconductors (*e.g.*, TiO<sub>2</sub>, FeTiO<sub>3</sub>, GdCrO<sub>3</sub>, and KTaO<sub>3</sub>) are intrinsic UV-light-driven photocatalysts, a more effective strategy would be to develop narrow-bandgap photocatalysts and thus utilize the whole solar spectrum. As a result, various chalcogenide materials (*e.g.*, CuInS<sub>2</sub><sup>77</sup> and CuFe<sub>0.7</sub>Cr<sub>0.3</sub>S<sub>2</sub><sup>78</sup>) have been developed. In particular, CuInS<sub>2</sub> has a narrow bandgap of 1.45 eV and an insufficient conduction band potential for H<sub>2</sub> production, thus preventing the over-reduction of nitrate to ammonia.

**2.1.2. Insights into the mechanism of ionic nitrogen oxide reduction.** The efficiency and selectivity of artificial solar denitrification systems can be increased by suppressing undesired reactions, which mainly correspond to DNRA (*i.e.*, ammonification) and the re-oxidation of NO<sub>2</sub><sup>−</sup> to NO<sub>3</sub><sup>−</sup>. In turn, a deep understanding of the overall mechanism is required to precisely control competitive reactions and thus selectively convert ionic nitrogen species to N<sub>2</sub> while maintaining sufficient catalytic rates for keeping up with the photon flux at maximum solar intensity. DNRA is widely known as the anaerobic microbial pathway of the natural nitrogen cycle. The important implication of DNRA in denitrification is the production of NH<sub>4</sub><sup>+</sup> from NO<sub>3</sub><sup>−</sup>, which is the major side reaction for the reduction of NO<sub>3</sub><sup>−</sup> to N<sub>2</sub>. The NO<sub>2</sub><sup>−</sup> ion produced by the reduction of NO<sub>3</sub><sup>−</sup> (NO<sub>3</sub><sup>−</sup> + 2e<sup>−</sup> + 2H<sup>+</sup> → NO<sub>2</sub><sup>−</sup> + H<sub>2</sub>O) can undergo ammonification (NO<sub>2</sub><sup>−</sup> + 6e<sup>−</sup> + 8H<sup>+</sup> → NH<sub>4</sub><sup>+</sup> + 2H<sub>2</sub>O) or denitrification (NO<sub>2</sub><sup>−</sup> + 6e<sup>−</sup> + 8H<sup>+</sup> → N<sub>2</sub> + 4H<sub>2</sub>O), both of which are six-electron reductions. The preference for a particular NO<sub>2</sub><sup>−</sup> reduction pathway is strongly affected by the environment, particularly by the ratio of N species to H atoms (N : H ratio) at active sites. The injection of excess H<sub>2</sub> increases the surface concentration of H<sup>+</sup> at active sites because of the low-energy-barrier dissociative adsorption of H<sub>2</sub> and thus increases the selectivity for NH<sub>4</sub><sup>+</sup> formation (Fig. 3a). Alternatively, the N : H ratio can be changed by controlling the steady-state concentration of NO<sub>2</sub><sup>−</sup> to increase the probability of binding of two nitrogen species to

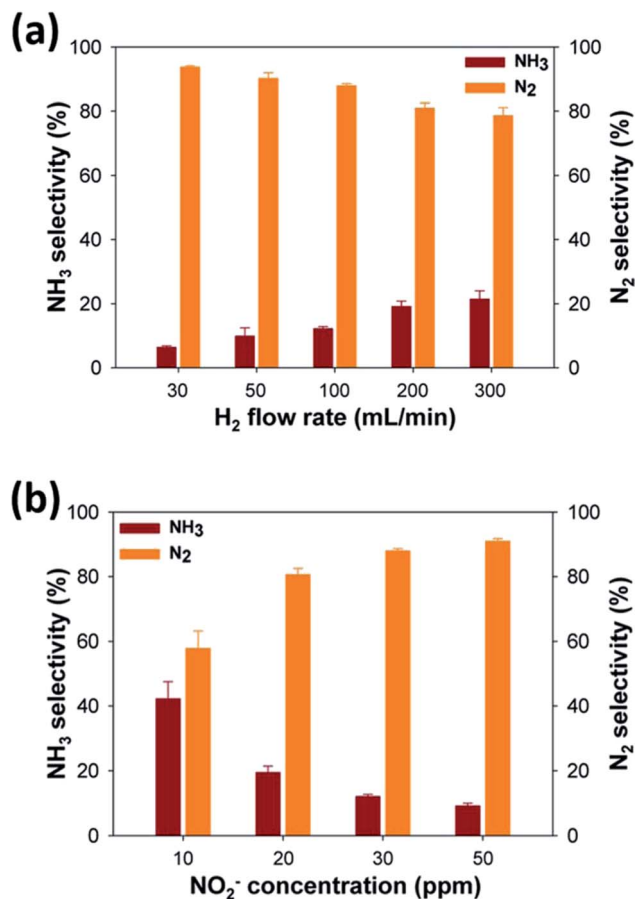


Fig. 3 Dependence of product ( $\text{N}_2$  and  $\text{NH}_3$ ) selectivity during  $\text{NO}_2^-$  reduction over  $\text{Pd/TiO}_2$  on (a)  $\text{H}_2$  flow rate and (b)  $\text{NO}_2^-$  concentration. Reprinted with permission from ref. 60. Copyright© 2014, American Chemical Society.

form  $\text{N}_2$  (Fig. 3b). The fine-tuning of the N : H ratio at surface active sites is required to suppress DNRA and thus selectively convert  $\text{NO}_2^-$  to  $\text{N}_2$ .

In the case of efficient nitrate conversion, photocatalytic nitrite oxidation, which is hard to detect during  $\text{NO}_3^-$  reduction, should be considered for low-efficiency nitrate reduction. Even if nitrification and denitrification occur simultaneously, it is difficult to identify the main factors of nitrification because of the same initial reactant and product. The formation of  $\text{NO}_3^-$  indicates that the oxidation of  $\text{NO}_2^-$  by holes occurs even in the presence of a hole scavenger in aqueous photocatalyst suspensions (Fig. 4). The low  $\text{NO}_3^-$  conversion efficiency is due to the low rate constant of  $\text{NO}_3^-$  reduction and the high rate constant of  $\text{NO}_2^-$  oxidation.

The minimal loss of photogenerated electron-hole pairs offers flexibility for maximizing photocatalytic efficiency by adding sacrificial hole or electron scavengers to restrict charge carrier recombination. Sacrificial electron donors (*i.e.*, hole scavengers) were used for photocatalytic denitrification in aqueous media to enable the efficient reduction of ionic nitrogen species<sup>5</sup> and were shown to affect reactant-photocatalyst interactions. Sacrificial reagents act not only as efficient

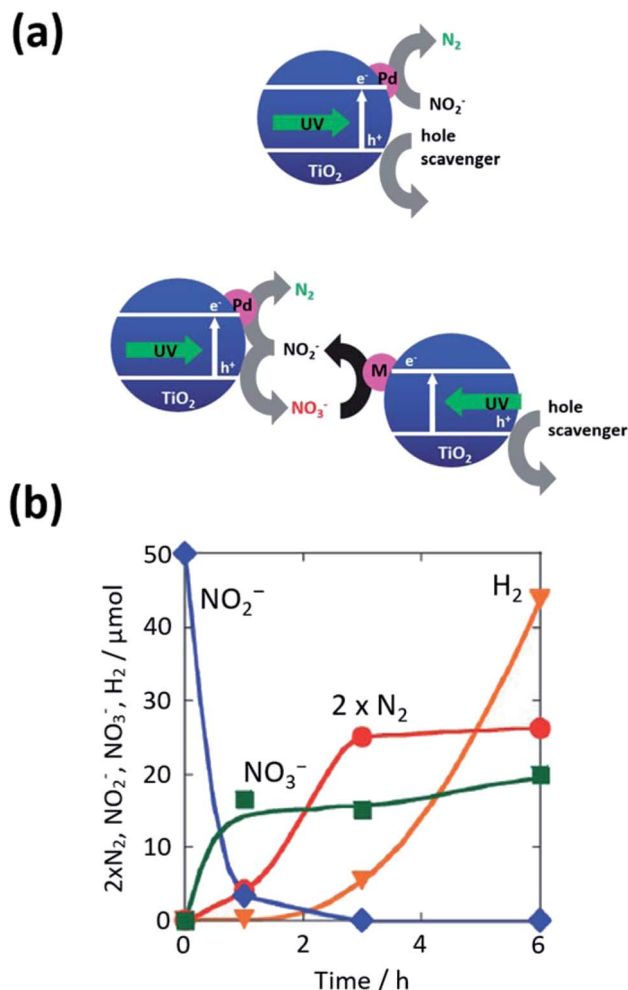


Fig. 4 (a) Schematic mechanism of  $\text{Pd/TiO}_2$  operation and the combination of two photocatalytic systems for the reduction of  $\text{NO}_2^-$  to  $\text{N}_2$  and  $\text{NO}_3^-$ . (b) Time-dependent conversion of  $\text{NO}_2^-$  and the formation of  $\text{N}_2$ ,  $\text{H}_2$ , and  $\text{NO}_3^-$  in suspensions of  $\text{Pd-TiO}_2$  in aqueous sodium oxalate (diamonds:  $\text{NO}_2^-$ , circles:  $\text{N}_2$ , squares:  $\text{NO}_3^-$ , triangles:  $\text{H}_2$ ). Reprinted with permission from ref. 29. Copyright© 2012, Royal Society of Chemistry.

hole scavengers but also as precursors of active radicals for ionic nitrogen oxide reduction. Sacrificial reagents were demonstrated to promote the efficient removal of holes and thus reduce charge carrier recombination while being oxidized<sup>34</sup> to afford strongly reducing ( $-1.81$  vs. SHE) carboxyl radicals ( $\text{CO}_2^{\cdot-}$ ), which also resulted in activity enhancement.<sup>79</sup> The most common sacrificial reagents are organic compounds such as formic acid,<sup>21,80,81</sup> oxalic acid,<sup>68,82,83</sup> humic acid,<sup>84</sup> and methanol.<sup>34</sup> Among them, formic acid is the best hole scavenger for  $\text{NO}_3^-$  reduction, as its simple structure results in the exclusive formation of the strongly reducing  $\text{CO}_2^{\cdot-}$ , while the release of protons promotes efficient  $\text{N}_2$ -selective reduction. Oxalic acid is the second most used hole scavenger, featuring a higher selectivity for  $\text{NH}_4^+$  formation than formic acid (Table 1). The dependence of selectivity on hole scavenger type is attributed to the reduction ability of the reactant and intermediates. Simple carboxyl compounds (formic acid, sodium

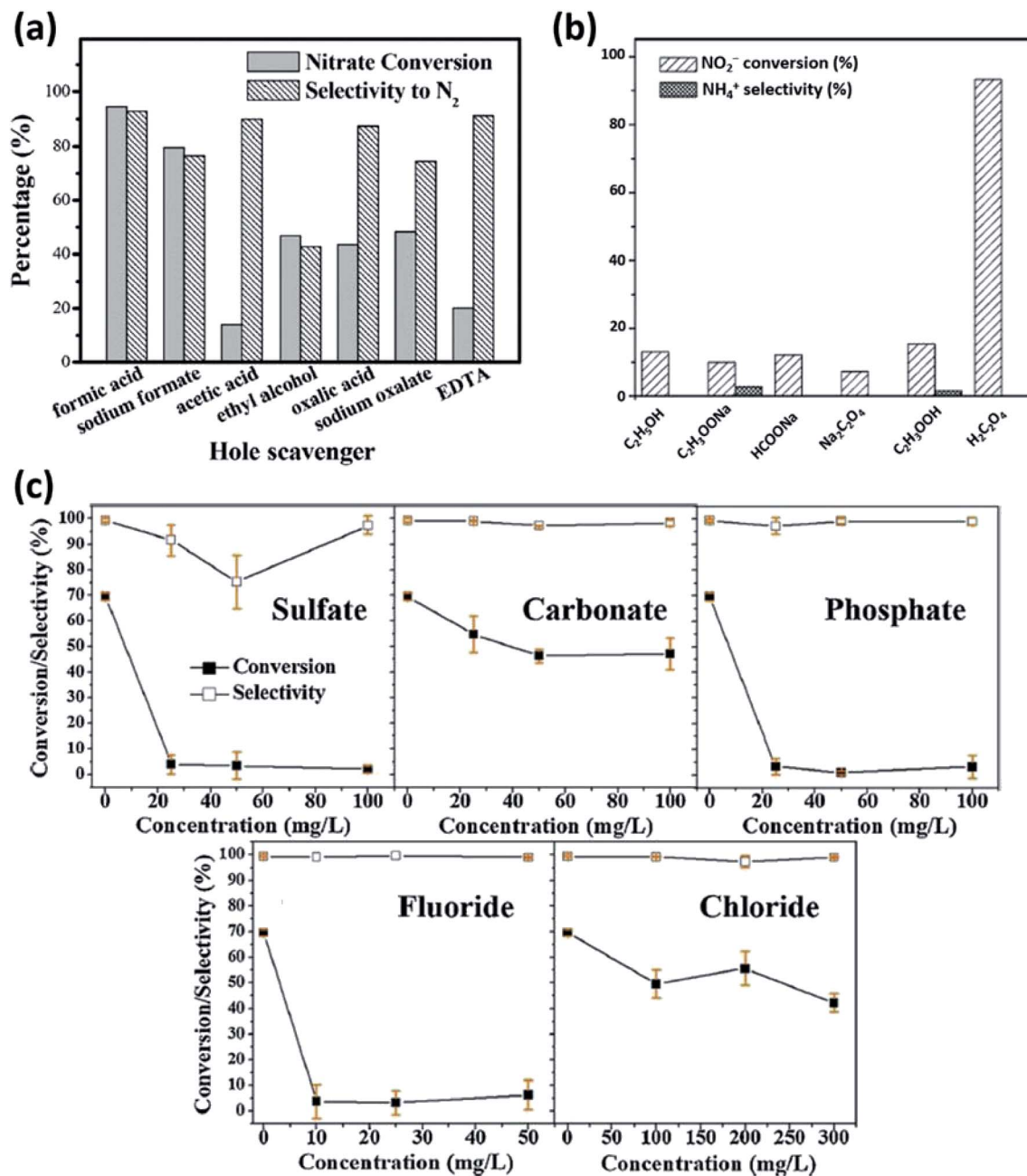


Fig. 5 (a) Effects of organic hole scavengers on the reduction of NO<sub>3</sub><sup>-</sup> over AgCl/TiO<sub>2</sub> nanotubes. Reprinted with permission from ref. 21. Copyright© 2018, Royal Society of Chemistry. (b) Effects of organic hole scavengers on the reduction of NO<sub>2</sub><sup>-</sup> over Ag/TiO<sub>2</sub>. Reprinted with permission from ref. 85. Copyright© 2007, American Chemical Society. (c) Photocatalytic nitrate conversion efficiency and N<sub>2</sub> selectivity achieved over TiO<sub>2</sub> in the presence of different levels of SO<sub>4</sub><sup>2-</sup>, HCO<sub>3</sub><sup>-</sup>, H<sub>2</sub>PO<sub>4</sub><sup>-</sup>, F<sup>-</sup> and Cl<sup>-</sup> (irradiation duration: 3 h, sacrificial agent: formic acid). Reprinted with permission from ref. 86. Copyright© 2020, Elsevier.

formate, etc.) are oxidized to afford abundant CO<sub>2</sub><sup>•-</sup> radicals and therefore allow for more efficient conversion than other organic hole scavengers. On the other hand, oxalic acid remarkably enhances the conversion of nitrite to N<sub>2</sub> while exhibiting a modest hole scavenging ability (Fig. 5a and b).<sup>21,85</sup> The understanding of the complicated interactions between various intermediates and sacrificial reagents is particularly challenging in the case of photocatalytic denitrification. In addition, the presence of additional reagents such as SO<sub>4</sub><sup>2-</sup>,

H<sub>2</sub>PO<sub>4</sub><sup>-</sup>, F<sup>-</sup>, Cl<sup>-</sup>, and HCO<sub>3</sub><sup>-</sup> increases system complexity and therefore leads to hole blocking and, as a consequence, inhibits hole scavenger oxidation by promoting surface anionization (Fig. 5c).<sup>86</sup>

## 2.2. Denitrification of airborne NO<sub>x</sub> and N<sub>2</sub>O to N<sub>2</sub>

Airborne nitrogen oxides (NO<sub>x</sub>) including NO and NO<sub>2</sub> originate from anthropogenic (combustion of fossil fuels at high



temperatures in automobile engines and power plants) and biogenic sources, significantly affecting human health and the environment.<sup>87</sup>  $\text{N}_2\text{O}$  is produced by human activities and natural processes and is both a greenhouse gas and an ozone-depleting substance.<sup>88</sup> Taken together,  $\text{NO}_x$  and  $\text{N}_2\text{O}$  significantly affect the environment *via* (i) ozone and smog generation due to the reaction of  $\text{NO}_x$  with volatile organic compounds (VOCs) upon irradiation with light, (ii) the acidification of water vapor (acid rain), (iii) excessive algal growth due to the dissolution of  $\text{NO}_x$  in water (eutrophication), (iv) climate change and ozone layer depletion, and (v) secondary fine dust formation through the combination of the above oxides with water vapor,  $\text{O}_3$ , ammonia, *etc.* Selective catalytic reduction (SCR)-based denitrification is a long-standing industrial process that is used to control air quality and is performed using different types of reactors and catalysts, depending on the application. Regarding the conventional  $\text{deNO}_x$  process, ammonia has been used as a reducing agent instead of hydrogen to improve process safety and reduce the operating temperature.<sup>89</sup> The conversion of  $\text{NO}_x$  to  $\text{N}_2$  is described by Eley–Rideal and Langmuir–Hinshelwood models, which rely on the decomposition of intermediates generated through the reaction of surface-adsorbed activated  $\text{NH}_3$  with free gaseous  $\text{NO}$  and  $\text{NO}$  adsorbed on basic catalyst sites, respectively. Alternatively, airborne  $\text{NO}_x$  can be removed *via* complete oxidation to  $\text{NO}_3^-$ . Although this approach (nitrification) has received widespread attention for the development of smart cement and asphalt used in the construction of the state-of-the-art urban infrastructure,<sup>90</sup> the accumulation of  $\text{NO}_3^-$  on the surface of photocatalysts can result in their deactivation. As this review focuses on denitrification only, readers interested in solar-driven nitrification are advised to consult appropriate literature.

The photocatalytic reduction of  $\text{NO}_x$  and  $\text{N}_2\text{O}$  to  $\text{N}_2$  offers the following advantages: (i) the use of water instead of the explosive  $\text{H}_2$  and the toxic  $\text{NH}_3$ , (ii) operation at standard temperature and pressure, (iii) net zero carbon emission for operation under natural sunlight, and (iv) the availability of cheap and environmentally benign materials.<sup>91–94</sup> As electron–hole pairs photogenerated in semiconducting materials can be transformed to the strongly oxidizing reactive oxygen species (ROS), aerobic conditions favor nitrification, in which case  $\text{O}_2$  acts as a good electron acceptor and a precursor of mobile hydroxyl radicals ( $\text{O}_2 + \text{H}^+ + \text{e}^- \rightarrow \text{HO}_2^\cdot$ ,  $\text{HO}_2^\cdot + \text{H}^+ + \text{e}^- \rightarrow \text{H}_2\text{O}_2$ ,  $\text{H}_2\text{O}_2 + \text{e}^- \rightarrow \text{OH}^- + \text{OH}^\cdot$ ).<sup>95</sup> Under anaerobic conditions, the electrons can be transferred to  $\text{NO}_x$  or  $\text{N}_2\text{O}$  without interference from  $\text{O}_2$  but can still be intercepted by water vapor ( $2\text{H}_2\text{O} + 2\text{e}^- \rightarrow \text{H}_2 + 2\text{OH}^-$ ) (Fig. 6). Ideally, the residual holes in photocatalysts oxidize water vapor ( $2\text{H}_2\text{O} + 4\text{h}^+ \rightarrow \text{O}_2 + 4\text{H}^+$ ), otherwise, nitrification is driven by oxidation with holes or  $\text{OH}^\cdot$  ( $\text{H}_2\text{O} + \text{h}^+ \rightarrow \text{OH}^\cdot + \text{H}^+$ ). Along with selective charge transfer, other problems such as low solar light absorption, poor catalytic activity, need for noble metal-based co-catalysts, and lack of long-term durability should be overcome for practical applications. Herein, we summarize the strategies (*e.g.*, structure and morphology control, co-catalyst loading, heteroatom doping, and hybridization with different types of materials) used to



Fig. 6 Comparison of photocatalytic nitrification (left panel) and denitrification (right panel) mechanisms. The bottom right panel presents  $\text{NH}_3$ -mediated denitrification, the release of trapped oxygen atoms from  $\text{NO}$  (green box), and the oxidation of sacrificial gases (purple box; ED stands for carbon-containing electron donors such as  $\text{CO}$ ,  $\text{CH}_4$ ,  $\text{C}_3\text{H}_8$ ,  $\text{CH}_3\text{OH}$ , and  $\text{C}_2\text{H}_5\text{OH}$ ).

address the weaknesses of the photocatalytic reduction of  $\text{NO}_x$  and  $\text{N}_2\text{O}$  to  $\text{N}_2$ .

### 2.2.1. Photocatalysts for the reduction of airborne $\text{NO}_x$ to $\text{N}_2$

*DeNO<sub>x</sub> without additional electron donors.* Water vapor and surface-trapped oxygen atoms formed by electron transfer to  $\text{NO}$  are ideal electron donors for the photocatalytic denitrification of  $\text{NO}_x$ ; however, the kinetics of water oxidation is sluggish, and the control of selective electron transfer to  $\text{NO}_x$  is difficult. Therefore, whereas most studies focus on photocatalyst structure/surface modification and the operation of  $\text{deNO}_x$  in the presence of nitrogen- or carbon-containing electron donors (*e.g.*,  $\text{NH}_3$ ,  $\text{CO}$ ,  $\text{CH}_4$ ,  $\text{C}_3\text{H}_8$ ,  $\text{CH}_3\text{OH}$ , and  $\text{C}_2\text{H}_5\text{OH}$ ), very few processes have been performed without these donors. Wu *et al.* optimized the selectivity of  $\text{NO}$  reduction to  $\text{N}_2$  by controlling oxygen vacancies in  $\text{TiO}_2$  nanoparticles.<sup>96</sup> These vacancies were introduced by doping the  $\text{TiO}_2$  lattice with  $\text{Fe}^{3+}$ , and the substitution of  $\text{Ti}^{4+}$  by  $\text{Fe}^{3+}$  contributed to the charge compensation between negatively charged dopants and positively charged oxygen vacancies.<sup>97</sup> In air, the photocatalytic conversion of  $\text{NO}$  over pristine  $\text{TiO}_2$  was not selective for  $\text{N}_2$  (Fig. 7a and Table 2), whereas a significantly improved selectivity was observed for  $\text{Fe}$ -doped  $\text{TiO}_2$  (Fig. 7b). The highest yield and selectivity for  $\text{N}_2$  were obtained under anaerobic conditions, and the formation of  $\text{NO}_2$  over  $\text{Fe}$ -doped  $\text{TiO}_2$  was completely suppressed (Fig. 7c). Thus, only  $\text{N}_2$  and  $\text{O}_2$  were detected along with unreacted  $\text{NO}$  in the outlet (Fig. 7d). The proposed mechanism (Table 3) is believed to involve ROS (superoxide anion radicals and hydroxyl radicals) as nitrification agents. On the other hand, oxygen vacancies stabilized by  $\text{Fe}$  doping enhanced selective charge transfer to  $\text{NO}$ , which did not involve radical species, providing a clue to the design of highly effective denitrification photocatalysts.

Likewise, according to Dong *et al.*,<sup>98</sup> the carbon vacancy tailoring of graphitic carbon nitride ( $g\text{-C}_3\text{N}_4$ ) nanosheets ( $\text{C}_v\text{-}g\text{-C}_3\text{N}_4$ ) significantly enhanced  $\text{NO}$  reduction under visible light irradiation (Fig. 8a). This reduction was faster in air than in

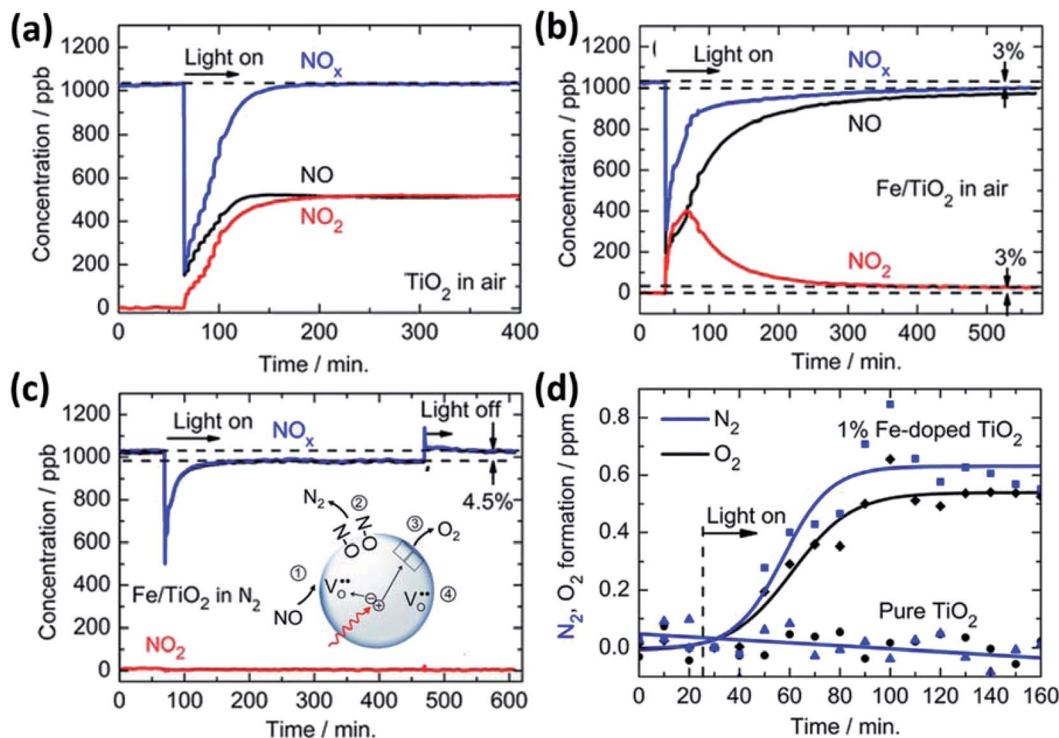


Fig. 7 Photocatalytic conversion of NO under UV light irradiation in air over (a) pristine TiO<sub>2</sub> and (b) Fe-doped TiO<sub>2</sub>. (c) Photocatalytic conversion of NO to N<sub>2</sub> over Fe-doped TiO<sub>2</sub> and the schematic mechanism of this conversion. The rapid decrease of NO in (a–c) is due to the formation of NO<sub>3</sub><sup>−</sup> via a reaction with superoxide anion radicals produced from adsorbed oxygen. (d) NO conversion ([NO] = 100 ppm) to N<sub>2</sub> and O<sub>2</sub> over pristine TiO<sub>2</sub> and Fe-doped TiO<sub>2</sub> in He. Reprinted with permission from ref. 96. Copyright© 2012, American Chemical Society.

argon irrespective of structure modification, as the ROS-mediated oxidation of NO to NO<sub>2</sub> is much more favorable under oxic conditions (Fig. 8b). While the photocatalytic removal of NO over g-C<sub>3</sub>N<sub>4</sub> was almost prohibited under anaerobic conditions, C<sub>v</sub>-g-C<sub>3</sub>N<sub>4</sub> was characterized by a relatively high conversion of NO and high selectivity for N<sub>2</sub> formation (Fig. 8c), as in the case of Fe-doped TiO<sub>2</sub>. In line with the enhanced light absorption of C<sub>v</sub>-g-C<sub>3</sub>N<sub>4</sub> and the restricted recombination of charge carriers therein, electron spin resonance (ESR) spectra suggested that surface adsorption sites stimulated the chemisorption of airborne NO (*via* the interaction between a carbon atom with an unpaired electron in g-C<sub>3</sub>N<sub>4</sub> and a nitrogen atom with an unpaired electron in NO), with carbon vacancies acting as active centers to induce interactions with the NO oxygen (*i.e.*, C<sub>v</sub>-O-N). Thus, after the adsorption of NO on g-C<sub>3</sub>N<sub>4</sub> and C<sub>v</sub>-g-C<sub>3</sub>N<sub>4</sub>, the ESR signal intensity due to carbon atoms with unpaired electrons decreased and increased, respectively (Fig. 8d and e). Illumination of C<sub>v</sub>-g-C<sub>3</sub>N<sub>4</sub> with pre-adsorbed NO induced a peak shift and the appearance of two new peaks at 3535 and 3555 G, which indicated the change of defect sites and the decomposition of NO into atomic N and O, respectively (Fig. 8f).

Prior to the strategies described above, Anpo *et al.* reported the UV light-promoted decomposition of NO into N<sub>2</sub> and O<sub>2</sub> over cation-exchanged ZSM-5 (Cu<sup>+</sup>, Ag<sup>+</sup>, and Pb<sup>2+</sup>),<sup>99–101</sup> vanadium silicate (VS)/ZSM-5,<sup>102</sup> and Ti-MCM-41.<sup>103</sup> Herein, we do not discuss the characteristics of such materials and the corresponding kinetic analysis in detail because of the multitude of

related reviews<sup>104–106</sup> but briefly overview the concept of transition metal ion-mediated electron transfer to NO. Cu<sup>+</sup> and Ag<sup>+</sup> immobilized in zeolites can be excited under illumination and transfer an electron to the π-antibonding orbital of NO while concomitantly accepting the electron of another NO molecule. Consequently, two contiguous N···O species adsorbed at metal ion sites are converted into N<sub>2</sub> and O<sub>2</sub>. Moreover, the coordination and distribution of metal oxide species, *e.g.*, four-fold tetrahedrally coordinated vanadium oxide species with a terminal oxovanadium group (V=O) in VS/ASM-5 and Ti oxide species with tetrahedrally coordinated Ti<sup>4+</sup> in Ti-MCM-41, strongly affected NO removal activity and selectivity. Although several studies demonstrated the selective conversion of NO to N<sub>2</sub> in the absence of supplements, the related yields were quite low, and the formation of undesired products could not be avoided, which was ascribed to catalyst inactivation *via* product accumulation on active sites. Another way to overcome this issue is the utilization of NH<sub>3</sub> and carbon-containing compounds as sacrificial molecules.

*DeNO<sub>x</sub> via NH<sub>3</sub>(g) oxidation.* The photo-assisted SCR (photo-SCR) of NO(g) with NH<sub>3</sub>(g) is an effective way to return N<sub>2</sub> to the atmosphere (4NO + 4NH<sub>3</sub> + O<sub>2</sub> → 4N<sub>2</sub> + 6H<sub>2</sub>O). Back in 1992, Cant *et al.* reported photo-SCR based on the reaction of NO with NH<sub>3</sub> over TiO<sub>2</sub> under UV light irradiation and used isotope labeling to elucidate the reaction pathway (4<sup>14</sup>N<sup>15</sup>N + 4<sup>15</sup>NH<sub>3</sub> + O<sub>2</sub> → 4<sup>14</sup>N<sup>15</sup>N + 6H<sub>2</sub>O).<sup>107</sup> In this system, NO removal was very slow, and N<sub>2</sub>O and NO<sub>3</sub><sup>−</sup> were still formed; moreover, the experiment was conducted under unrealistic conditions. Over

Table 2 Performances of various materials as photocatalysts for the denitrification of airborne NO<sub>x</sub>

No.	Photocatalyst	Target (Conc.)	Light	Temp.	Flow rate & GHSV	Carrier gas	Supplements	NO conversion (%)	N <sub>2</sub> selectivity (%)	By-products	Ref.
1	TiO <sub>2</sub>	NO (1000 ppb)	UV	r.t.	1 L min <sup>-1</sup>	Air	None	~50	—	NO <sub>2</sub> , NO <sub>3</sub> <sup>-</sup>	96
2	Fe-doped TiO <sub>2</sub>					Air		~6	~50	NO <sub>2</sub> , NO <sub>3</sub> <sup>-</sup>	
3	g-C <sub>3</sub> N <sub>4</sub>	NO (600 ppb)	Visible (420 nm ≤)	r.t.	1 L min <sup>-1</sup>	N <sub>2</sub>	None	~4.5	~100	NO <sub>2</sub> , NO <sub>3</sub> <sup>-</sup>	98
4						Air		~38	—	NO <sub>2</sub> , undefined	
5		NO (1500 ppb)				Ar		Almost negligible	—	—	
6	g-C <sub>3</sub> N <sub>4</sub> with carbon vacancies	NO (600 ppb)				Air		~48	—	NO <sub>2</sub> , undefined	
7		NO (1500 ppb)				Ar		~34	~66	NO <sub>2</sub> , undefined	
8	Cu <sup>+</sup> -ZSM-5	NO (2 Torr)	UV (280 nm <)	r.t.	—	—	None	~2 (4 h)	~100	—	99
9	Ti-MCM-41	NO (180 μmol Eg-cat <sup>-1</sup> )	UV (240 nm <)	r.t.	—	—	None	~1.1 (1 h)	~75	N <sub>2</sub> O, undefined	103
10	JCR-TiO <sub>2</sub> (anatase)	NO (1000 ppm)	UV	r.t.	GHSV 32 000 h <sup>-1</sup>	2% O <sub>2</sub> , 98% Ar	NH <sub>3</sub> (1000 ppm)	41	100	—	108
11	JCR-TiO <sub>2</sub> (rutile)							53	100	—	
12	JCR-TiO <sub>2</sub> (anatase 91.3% + rutile 8.7%)							63	100	—	
13	V <sub>2</sub> O <sub>5</sub> /TiO <sub>2</sub> (1 wt%)	NO (1000 ppm)	UV	r.t.	GHSV 50 000 h <sup>-1</sup>	2% O <sub>2</sub> , 98% Ar	NH <sub>3</sub> (1000 ppm)	17.7	100	—	114
14	CrO <sub>6</sub> /TiO <sub>2</sub> (1 wt%)							34.2	100	—	
15	MnO/TiO <sub>2</sub> (1 wt%)							12.1	100	—	
16	Fe <sub>2</sub> O <sub>3</sub> /TiO <sub>2</sub> (1 wt%)							29.6	100	—	
17	CoO/TiO <sub>2</sub> (1 wt%)							21.6	100	—	
18	NiO/TiO <sub>2</sub> (1 wt%)							27.0	100	—	
19	CuO/TiO <sub>2</sub> (1 wt%)							26.1	100	—	
20	ZnO/TiO <sub>2</sub> (1 wt%)							46.6	100	—	
21	Y <sub>2</sub> O <sub>3</sub> /TiO <sub>2</sub> (1 wt%)							47.0	100	—	
22	ZrO <sub>2</sub> /TiO <sub>2</sub> (1 wt%)							41.1	100	—	
23	Nb <sub>2</sub> O <sub>5</sub> /TiO <sub>2</sub> (1 wt%)							58.4	>99	—	
24	MoO <sub>3</sub> /TiO <sub>2</sub> (1 wt%)							60.2	>99	—	
25	Ta <sub>2</sub> O <sub>5</sub> /TiO <sub>2</sub> (1 wt%)							38.6	100	—	
26	WO <sub>3</sub> /TiO <sub>2</sub> (1 wt%)							63.6	>99	—	
27	N3-dye TiO <sub>2</sub>	NO (1000 ppm)	Visible (420 nm ≤)	r.t.	GHSV 100 000 h <sup>-1</sup>	2% O <sub>2</sub> , 98% He	NH <sub>3</sub> (1000 ppm)	>99	>99	—	121
28	LaFe <sub>0.4</sub> Mn <sub>0.6</sub> O <sub>3</sub> /attapulgite	NO (1000 ppm)	UV	r.t.	GHSV 50 000 h <sup>-1</sup>	3% O <sub>2</sub> , 97% N <sub>2</sub>	NH <sub>3</sub> (1000 ppm)	~85	~100	—	122
29	La <sub>0.7</sub> Ce <sub>0.3</sub> FeO <sub>3</sub> /attapulgite	NO (1000 ppm)	UV	r.t.	0.1 L min <sup>-1</sup>	3% O <sub>2</sub> , 97% N <sub>2</sub>	NH <sub>3</sub> (1000 ppm)	~80	—	—	123
30	LaFe <sub>0.5</sub> Ni <sub>0.5</sub> O <sub>3</sub> /palygorskite	NO (1000 ppm)	Visible (420 nm ≤)	200 °C	GHSV 50 000 h <sup>-1</sup>	3% O <sub>2</sub> , 97% N <sub>2</sub>	NH <sub>3</sub> (1000 ppm)	~92	~98	—	124
31	La <sub>0.5</sub> Pr <sub>0.5</sub> CoO <sub>3</sub> /palygorskite	NO (1000 ppm)	Visible (420 nm ≤)	200 °C	GHSV 40 000 h <sup>-1</sup>	3% O <sub>2</sub> , 97% N <sub>2</sub>	NH <sub>3</sub> (1000 ppm)	~95	~99	—	125
32	N-doped carbon quantum dot	NO (1000 ppm)	Visible	150–200 °C	GHSV 50 000 h <sup>-1</sup>	3% O <sub>2</sub> , 97% N <sub>2</sub>	NH <sub>3</sub> (1000 ppm)	~93	100	—	127

Table 2 (Contd.)

No.	Photocatalyst	Target (Conc.)	Light	Temp.	Flow rate & GHSV	Carrier gas	Supplements	NO conversion (%)	N <sub>2</sub> selectivity (%)	By-products	Ref.
33	modified PrFeO <sub>3</sub> / palygorskite Fe <sub>2</sub> O <sub>3</sub> /SmFeO <sub>3</sub> / palygorskite	NO (1000 ppm)	UV	<200 °C	GHSV 40 000 h <sup>-1</sup>	3% O <sub>2</sub> , 97% N <sub>2</sub>	NH <sub>3</sub> (1000 ppm)	~95	100	—	128
34	palygorskite LaCoO <sub>3</sub> / appapulgite/rGO	NO (1000 ppm)	UV	100–150 °C	GHSV 50 000 h <sup>-1</sup>	3% O <sub>2</sub> , 97% N <sub>2</sub>	NH <sub>3</sub> (1000 ppm)	~95	100	—	129
35	Ag/TiO <sub>2</sub> (1 wt%)	NO (909 ppm)	UV	r.t.	5.5 cm <sup>3</sup> min <sup>-1</sup>	Ar	CO (1818 ppm)	~35 μmol h <sup>-1</sup> g <sup>-1</sup> cat <sup>-1</sup>	90	—	136
36	Ag/TiO <sub>2</sub> (5 wt%)	—	—	—	—	—	—	~10 μmol h <sup>-1</sup> g <sup>-1</sup> cat <sup>-1</sup>	100	—	150
37	TiO <sub>2</sub>	NO (3000 ppm)	UV	150 °C	—	5% O <sub>2</sub> , 3% H <sub>2</sub> O in N <sub>2</sub>	Carbon black	97	99	N <sub>2</sub> O	150

Table 3 Proposed mechanism for the conversion of NO on pristine and Fe-doped TiO<sub>2</sub>.<sup>96</sup>

Byproduct ( <i>i.e.</i> , NO <sub>2</sub> and NO <sub>3</sub> <sup>-</sup> ) formation over TiO <sub>2</sub>	
[Reductive pathway]	[Oxidative pathway]
Superoxide radical-mediated	Hydroxyl radical-mediated
Ti(O <sub>2</sub> ) <sub>ads</sub> + e <sup>-</sup> → Ti(O <sub>2</sub> <sup>-</sup> ) <sub>ads</sub>	Ti-OH <sup>-</sup> + h <sup>+</sup> → Ti-OH <sup>•</sup>
Ti(O <sub>2</sub> <sup>-</sup> ) <sub>ads</sub> + NO(g) → Ti(NO <sub>3</sub> <sup>-</sup> ) <sub>ads</sub>	Ti-OH <sup>•</sup> + NO(g) → Ti-H + NO <sub>2</sub> (g)
Ti(O <sub>2</sub> ) <sub>ads</sub> + Ti-OH <sup>-</sup> + hν + 2NO(g) → Ti(NO <sub>3</sub> <sup>-</sup> ) <sub>ads</sub> + Ti-H + NO <sub>2</sub> (g)	

<sup>a</sup>Conversion of NO to N<sub>2</sub> over Fe-doped TiO<sub>2</sub>

[Reductive pathway]	[Oxidative pathway]
V <sub>O(surf)</sub> <sup>•</sup> + 2e <sup>-</sup> + NO(g) → O <sub>surf</sub> - N (1)	V <sub>O</sub> <sup>x</sup> + 2h <sup>+</sup> → V <sub>O</sub> <sup>••</sup> (4)
2O <sub>surf</sub> -N → 2O <sub>surf</sub> + N <sub>2</sub> (g) (2)	
2O <sub>surf</sub> → O <sub>2</sub> (g) (3)	
2NO(g) + 4hν → N <sub>2</sub> (g) + O <sub>2</sub> (g)	

<sup>a</sup> Numbers 1–4 denote the reaction pathway numbered in the scheme of Fig. 7c. V<sub>O</sub><sup>•</sup> and V<sub>O</sub><sup>••</sup> denote charged and neutral oxygen vacancies, respectively.

the past 20 years, Tanaka's group systematically investigated the photo-SCR of NO, mainly focusing on the synthesis of TiO<sub>2</sub>-based photocatalysts, reaction mechanism verification, and the design of flow-type photoreactors operable at high gas hourly space velocities (GHSV).<sup>108,109</sup> From a mechanistic point of view, the photo-SCR of NO over TiO<sub>2</sub> photocatalysts is suggested to comprise five steps (Fig. 9a).<sup>110,111</sup> According to this mechanism, NH<sub>3</sub>(g) is adsorbed on the Lewis-acidic sites of TiO<sub>2</sub> (step 1) and is then oxidized by a photogenerated hole (step 2), while the photogenerated electron is trapped by Ti<sup>4+</sup>. The adsorbed NH<sub>2</sub><sup>•</sup> reacts with NO(g) through the Eley-Rideal mechanism (step 3), and the nitrosoamide (NH<sub>2</sub>NO) formed as an intermediate decomposes into N<sub>2</sub> and H<sub>2</sub>O (step 4). The remaining Ti<sup>3+</sup> is oxidized by electron transfer to O<sub>2</sub>(g) to regenerate Ti<sup>4+</sup> (step 5). As NH<sub>3</sub> adsorption takes place on Lewis-acidic sites, surface acidity control is an effective way of improving photo-SCR performance, whereas non-acidic surface area and the crystal phase do not contribute to activity enhancement.<sup>112</sup> The rate-limiting step is affected by the concentration of O<sub>2</sub>, corresponding to step 4 in the presence of excess O<sub>2</sub> and step 5 at O<sub>2</sub> contents of <2 vol%. Ji *et al.*<sup>113</sup> suggested that (i) the adsorption of NH<sub>3</sub> and its direct oxidation by photogenerated holes was preferred to the dissociative adsorption of NH<sub>3</sub> on TiO<sub>2</sub>, as proton-coupled hole transfer was energetically favored (NH<sub>3</sub> + h<sup>+</sup> + O<sub>2f</sub><sup>-</sup> → NH<sub>2</sub><sup>•</sup> + O<sub>2f</sub>H<sup>-</sup>; O<sub>2f</sub> denotes a two-fold coordinated O atom in TiO<sub>2</sub>) and the formation of NH<sub>2</sub>NO proceeded *via* the Eley-Rideal mechanism, and (ii) the decomposition of NH<sub>2</sub>NO into N<sub>2</sub> and O<sub>2</sub> was initiated by the transfer of H<sub>b</sub> to the O atom, which was followed by either the transfer of H<sub>a</sub> to O-H<sub>b</sub> or the transfer of O-H<sub>b</sub> to the surface Ti atom (Fig. 9b). Step 4 was calculated to have the highest energy barrier among other steps (*i.e.*, it was the rate-limiting step), in line with the experimental result of Tanaka's group.

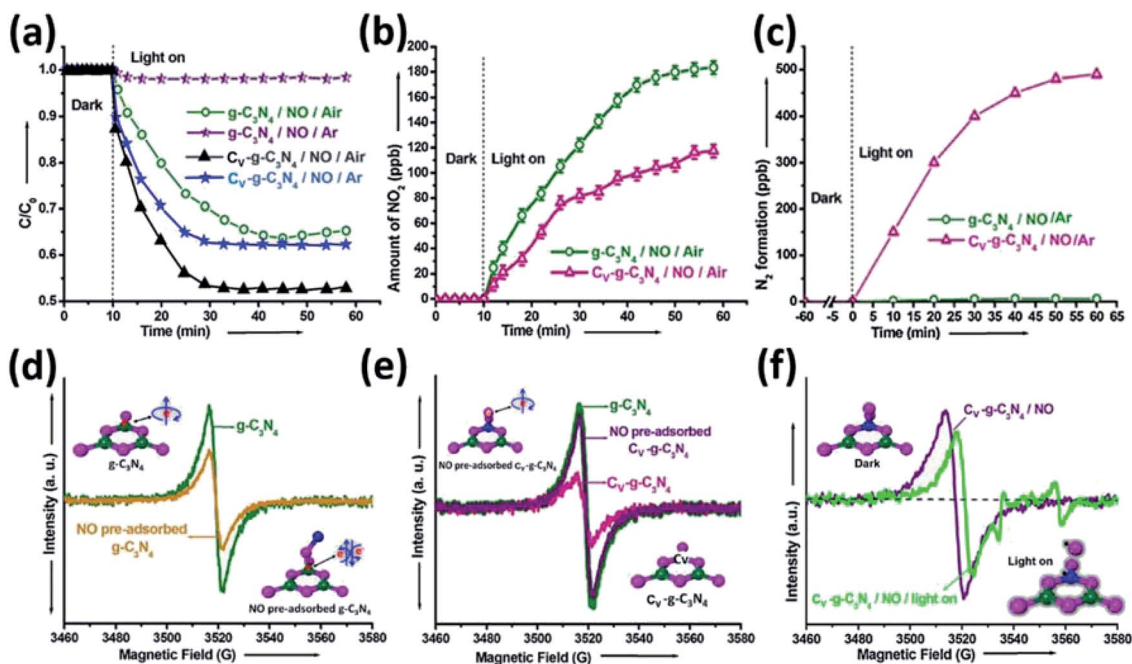


Fig. 8 (a) Photocatalytic removal of NO ([NO] = 1500 ppb) in air and argon over  $g\text{-C}_3\text{N}_4$  and  $\text{C}_v\text{-}g\text{-C}_3\text{N}_4$  under UV light irradiation. Production of (b)  $\text{NO}_2$  in air and (c)  $\text{N}_2$  in argon over  $g\text{-C}_3\text{N}_4$  and  $\text{C}_v\text{-}g\text{-C}_3\text{N}_4$ . ESR spectra of (d)  $g\text{-C}_3\text{N}_4$  and (e)  $\text{C}_v\text{-}g\text{-C}_3\text{N}_4$  before and after NO adsorption. (f) ESR spectra of  $\text{C}_v\text{-}g\text{-C}_3\text{N}_4$  with adsorbed NO recorded in the dark and under UV light irradiation. Reprinted with permission from ref. 98. Copyright© 2017, Elsevier.

To realize high catalytic performance or to run the system under visible light, one should appropriately design or modify the photocatalysts. Herein, photocatalysts were classified as those based on  $\text{TiO}_2$  or other materials. When  $\text{TiO}_2$  was modified with transition metal (V, Cr, Mn, Fe, Co, Ni, Cu, Zn, Y, Zr, Nb, Ta, and W) oxides, increased NO conversion was observed only for the more acidic  $\text{ZnO}$ ,  $\text{Y}_2\text{O}_3$ ,  $\text{Nb}_2\text{O}_5$ ,  $\text{MoO}_3$ , and  $\text{WO}_3$  (Fig. 10a and Table 2).<sup>114</sup> The low activity observed for other oxides was ascribed to their non-photocatalytic nature or the instability of active sites. The highest activity of  $\text{WO}_3/\text{TiO}_2$  was attributed to the facile decomposition of  $\text{NH}_2\text{NO}$  on the weakly Lewis-acidic sites of  $\text{WO}_3$ .<sup>115</sup> The doping of Si into  $\text{TiO}_2$  caused the formation of smaller crystals with a higher surface area and pore volume, and acidity was enhanced because of the increased concentration of surface hydroxyl groups.<sup>116</sup> The morphology of  $\text{TiO}_2$  was tailored by Ti foil anodization, and high-aspect-ratio  $\text{TiO}_2$  nanotubes provided more sites for  $\text{NH}_3$  adsorption than spherical  $\text{TiO}_2$  (P25).<sup>117</sup> Although  $\text{TiO}_2$  does not absorb visible light, the adsorption of  $\text{NH}_3$  on  $\text{TiO}_2$  could generate an extra energy level in the bandgap *via in situ* doping to induce direct electron transfer from the N 2p orbital to the Ti 3d orbital under irradiation with visible light ( $\lambda \geq 400$  nm).<sup>118</sup> This concept resembles that of ligand-to-metal charge transfer.<sup>119</sup> Dye sensitization is an effective way to inject electrons from dye molecules into the conduction band of  $\text{TiO}_2$  under visible light. Among the 15 dyes anchored on  $\text{TiO}_2$ , the  $\text{Ru}(2,2'\text{-bipyridyl-4,4'-dicarboxylic acid})_2(\text{NCS})_2$  complex (N3-dye) showed the highest performance (Fig. 10b).<sup>120,121</sup> The remaining holes in the HOMOs of dye molecules activated  $\text{NH}_3$ , and  $\text{N}_2$  was selectively formed by the reaction between  $\text{NO}_2^-$  and  $\text{NH}_2^-$ .

Consequently, the complete conversion of NO and a 100% selectivity for  $\text{N}_2$  were achieved at a high GHSV of  $100\,000\text{ h}^{-1}$  under 30 min irradiation with visible light (Table 2). One of the serious problems of dye-sensitized systems in aqueous media is the detachment of dye molecules from  $\text{TiO}_2$  and the dependence of charge transfer on the complexation between functional groups. However, the occurrence of the reaction at the gas–solid interface allows dye desorption to be ignored. Therefore, numerous dyes are available for dye-sensitized SCR.

Yao's group designed diverse types of photocatalytic systems for the photo-SCR of NO, mainly those relying on (i) cascaded electron transfer [ $\text{LaFe}_{1-x}\text{Mn}_x\text{O}_3/\text{palygorskite}$ ,<sup>122</sup>  $\text{La}_{1-x}\text{Ce}_x\text{FeO}_3/\text{palygorskite}$ ,<sup>123</sup>  $\text{LaFe}_{1-x}\text{Ni}_x\text{O}_3/\text{palygorskite}$ ,<sup>124</sup>  $\text{La}_{1-x}\text{Pr}_x\text{CoO}_3/\text{palygorskite}$ ,<sup>125</sup>  $\text{CaTi}_{1-x}\text{Mn}_x\text{O}_{3-\delta}$ ,<sup>126</sup>], (ii) Z-scheme electron transfer [ $\text{N-doped carbon quantum dots}/\text{PrFeO}_3$ ,<sup>127</sup>  $\text{Fe}_2\text{O}_3/\text{SmFeO}_3/\text{palygorskite}$ ,<sup>128</sup>  $\text{LaCoO}_3/\text{palygorskite}/\text{reduced graphene oxide}$ ,<sup>129</sup>  $\text{Pr}_{1-x}\text{Ce}_x\text{FeO}_3/\text{palygorskite}$ ,<sup>130</sup>  $\text{CeVO}_4/\text{modified palygorskite}$ ,<sup>131</sup>], and (iii) up-conversion (near-infrared light  $\rightarrow$  UV and visible light) [ $\text{CeO}_2/\text{Pr}^{3+}/\text{palygorskite}$ ,<sup>132</sup> and  $\text{CeO}_2/\text{palygorskite}$ ,<sup>133</sup>] (Fig. 11 and Table 2). The metal ion content and hetero-element doping in mixed oxides altered the photocatalyst's physical properties such as particle size, electronic band structure, surface acidity, and charge trapping sites, and the supports (palygorskite) were shown to prevent nanoparticle agglomeration and provide sites for  $\text{NH}_3$  adsorption. High NO conversion and the selective formation of  $\text{N}_2$  were achieved, and the mechanism of NO conversion to  $\text{N}_2$  was the same as that reported by Tanaka's group despite the difference in electron transfer pathways proposed. The Ag nano- and sub-nano-clusters incorporated in zeolites also promoted photo-assisted

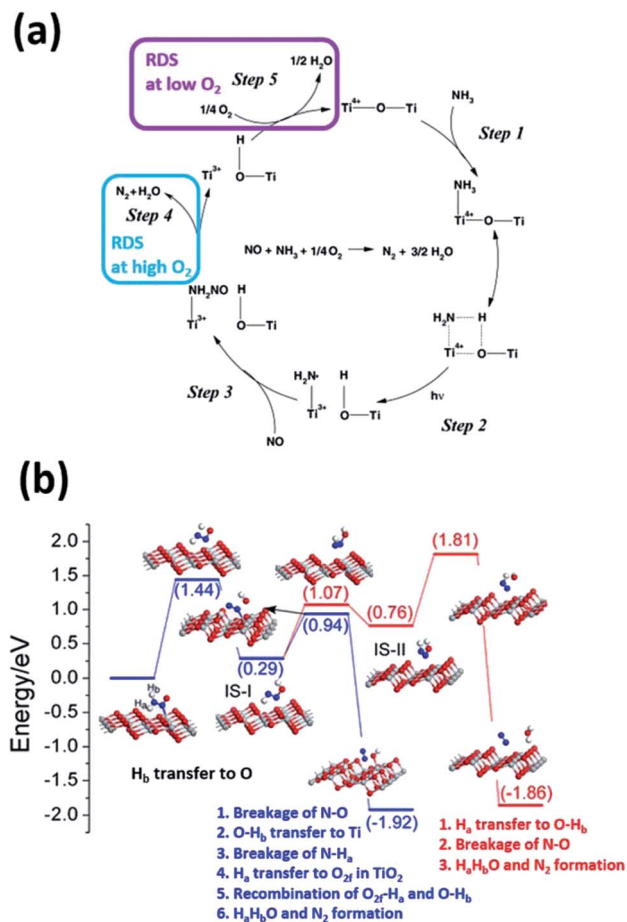


Fig. 9 (a) Mechanism of the photocatalytic reduction of NO by NH<sub>3</sub> over TiO<sub>2</sub>. Reprinted with permission from ref. 111. Copyright© 2004, Elsevier. (b) Potential energy diagram for the decomposition of NH<sub>2</sub>NO on the (101) surface of anatase TiO<sub>2</sub>. Reprinted with permission from ref. 113. Copyright© 2014, American Chemical Society.

SCR under visible light irradiation ( $\lambda \geq 390$  nm), with activity determined by the reaction temperature (room temperature *vs.* 150 °C).<sup>134</sup> Ag<sub>n</sub><sup>δ+</sup> clusters were utilized as sensitizers because of their surface plasmon resonance and they favored the decomposition of NH<sub>2</sub>NO to N<sub>2</sub> at 150 °C as opposed to the further oxidation of NH<sub>2</sub> to NO and then to NO<sub>2</sub> by singlet oxygen at room temperature.

*DeNO<sub>x</sub> via the oxidation of carbon-containing compounds.* NH<sub>3</sub> can be replaced by CH<sub>4</sub>, C<sub>3</sub>H<sub>8</sub>, C<sub>4</sub>H<sub>10</sub>, CO, CO(NH<sub>2</sub>)<sub>2</sub>, C<sub>2</sub>H<sub>5</sub>OH, carbon black, *etc.* for the photo-SCR of NO to N<sub>2</sub> over TiO<sub>2</sub>-based catalysts under aerobic conditions. Bowering *et al.* tested the photocatalytic conversion of NO to N<sub>2</sub> over TiO<sub>2</sub> (P25) in the presence of CO as a reducing agent under UV light irradiation and showed that the reaction did not follow the Eley-Rideal mechanism but was rather driven by the adsorbed CO and NO (*i.e.*, (i) CO<sub>ads</sub> + O<sub>ads</sub> → CO<sub>2</sub>(g); (ii) CO<sub>ads</sub> + 2NO<sub>ads</sub> → N<sub>2</sub>O<sub>ads</sub> + CO<sub>2ads</sub>; (iii) CO<sub>ads</sub> + N<sub>2</sub>O<sub>ads</sub> → N<sub>2</sub>(g) + CO<sub>2ads</sub>).<sup>135</sup> Therefore, the rate of NO conversion was the highest under CO-free conditions owing to the absence of competitive adsorption, whereas the highest selectivity for N<sub>2</sub> was achieved in the presence of CO even though NO conversion was reduced. In the latter case, the



Fig. 10 (a) Photo-SCR of NO over various metal oxide (1.0 wt%) promoted TiO<sub>2</sub> (GHSV: 50 000 h<sup>-1</sup>). (b) Photo-SCR of NO over dye-modified TiO<sub>2</sub> under visible light irradiation (dye loading: 12.5 μmol g<sup>-1</sup>, GHSV: 100 000 h<sup>-1</sup>). (1) N3 dye, (2) Rose Bengal, (3) eosin Y, (4) Ru(bpy)<sub>3</sub>Cl<sub>2</sub>, (5) rhodamine B, (6) coumarin 343, (7) TCPP, (8) methylene blue, (9) Zn phthalocyanine, (10) Congo Red, (11) phthalocyanine, (12) RhCl<sub>3</sub>, (13) Indigo Carmine, (14) Cu phthalocyanine, and (15) carmine dyes. Reprinted with permission from ref. 109 and 121. Copyright© 2016 and 2015, Wiley.

surface hydroxyl groups significantly influenced selectivity (more hydroxyl groups led to better performance), and the loading of Ag on TiO<sub>2</sub> markedly enhanced selectivity while reducing NO conversion, as Ag clusters acted as centers for electron-hole pair recombination.<sup>136</sup> The electron defects (Ti<sup>3+</sup>, F<sup>+</sup>, and F centers) intentionally introduced on TiO<sub>2</sub> by partial reduction could reduce NO under visible light irradiation, and the presence of CO as a regenerator of donor centers increased the selectivity for N<sub>2</sub>.<sup>137</sup> Although extra experiments were also performed in the presence of hydrocarbons such as C<sub>2</sub>H<sub>6</sub>, C<sub>2</sub>H<sub>4</sub>, C<sub>3</sub>H<sub>8</sub>, propylene, C<sub>4</sub>H<sub>10</sub>, benzene, toluene, ethylbenzene, and *o*-xylene, the research goal was not the selective conversion of NO to N<sub>2</sub> but the utilization of NO as an oxidant for the removal of VOC.<sup>138,139</sup>

Wu's group employed photo-SCR for denitrification in the presence of saturated hydrocarbons including CH<sub>4</sub>.<sup>140,141</sup>

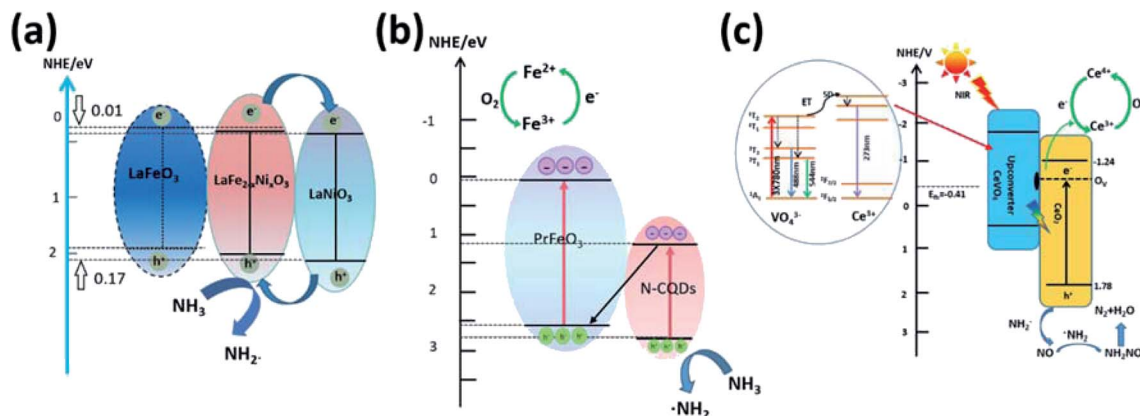


Fig. 11 Schematic diagrams of (a) cascaded electron transfer, (b) Z-scheme electron transfer, and (c) electron transfer in composite materials for the photocatalytic oxidation of  $\text{NH}_3$ . Reprinted with permission from ref. 124 and 133. Copyright© 2018 and 2020, Elsevier. Reprinted with permission from ref. 127. Copyright© 2018, American Chemical Society.

$\text{C}_3\text{H}_8$ ,<sup>142–144</sup> and  $\text{C}_4\text{H}_{10}$ <sup>145–147</sup> as reducing agents, focusing on the synthesis of  $\text{TiO}_2$  and its structure/surface modification in  $\text{Pd}/\text{TiO}_2$ ,  $\text{PtO}_x\text{PdO}_y/\text{TiO}_2$ ,  $\text{PdO}/\text{TiO}_2$ ,  $\text{Ag}/\text{TiO}_2$ ,  $\text{Cu}/\text{TiO}_2$ ,  $\text{Pt}/\text{TiO}_2$ , and  $\text{TiO}_2$  nanosheets. In the absence of co-catalysts on  $\text{TiO}_2$ , the electron-donating behavior of hydrocarbons was not effectively utilized, unlike in the case of  $\text{NH}_3$ . However, the temperature and the presence of moisture and oxygen were important for controlling  $\text{NO}$  conversion and selectivity for  $\text{N}_2$ . For example, when  $\text{PtO}_x\text{PdO}_y/\text{TiO}_2$  was tested at temperatures of 25, 70, and 120 °C, the best performance was observed at the highest temperature when either oxygen or water vapor was present, as these conditions helped to avoid the accumulation of nitrate and the desorption of water vapor from active sites, respectively. On the other hand, the opposite trend was observed under vapor- and oxygen-free conditions because of the poor adsorption of  $\text{C}_3\text{H}_8$  and  $\text{NO}$  (competitive adsorption as in the case of  $\text{CO}$ ) on the catalyst surface at high temperature. Without  $\text{PtO}_x\text{PdO}_y$  catalysts,  $\text{NO}$  oxidation was dominant, and therefore, nitrate was formed as the major product, with its accumulation on the surface resulting in a decrease of activity with reaction time.

The utilization of urea,  $\text{C}_2\text{H}_5\text{OH}$ , and carbon black as reducing agents was also possible for the photocatalytic denitrification of  $\text{NO}$  to  $\text{N}_2$ . In the case of  $\text{TiO}_2$  and urea co-supported carbon fiber,  $\text{TiO}_2$  and urea promoted the formation of  $\text{NO}_2$  and the sequential reduction of  $\text{NO}_2$  to  $\text{N}_2$  at room temperature, respectively, with moisture accelerating the desorption of  $\text{NO}_2$  from  $\text{TiO}_2$ .<sup>148</sup> In the case of  $\text{Au}/\text{TiO}_2$  + ethanol, the adsorption and dissociation of ethanol on Au particles or at the  $\text{Au}/\text{TiO}_2$  interface initiated the reaction at room temperature when  $\text{C}_2\text{H}_5\text{O}_{\text{ads}}$  accepted a photogenerated electron. This reaction was also promoted by the by-products ( $\text{CH}_3\text{CHO}$ ,  $\text{H}_2$ ,  $\text{CO}$ , and  $\text{CH}_4$ ) formed by ethanol decomposition.<sup>149</sup> Last, the reduction of  $\text{NO}$  to  $\text{N}_2$  was conducted over  $\text{TiO}_2$  along with the photocatalytic oxidation of carbon black to  $\text{CO}_2$  in the presence of  $\text{O}_2$  and moisture at 150 °C, providing the possibility of utilizing solid materials as reductants (Table 2).<sup>150</sup>

**2.2.2. Photocatalytic removal of  $\text{N}_2\text{O}(\text{g})$  to  $\text{N}_2$ .** Several decades ago, the photocatalytic denitrification of  $\text{N}_2\text{O}$  to  $\text{N}_2$  was investigated on  $\text{ZnO}$  at 371–431 °C under UV light irradiation, which induced the decomposition of  $\text{N}_2\text{O}$  via a combination of thermocatalysis and photocatalysis.<sup>151</sup> The thermocatalytic reaction followed first-order kinetics, while the photocatalytic reaction kinetics was more complicated and governed by  $\text{N}_2\text{O}^-$  that was formed as an intermediate through electron transfer from  $\text{ZnO}$  to  $\text{N}_2\text{O}$ . The mechanism proposed for n-type metal oxides in the dark at 20 °C comprises five steps and features step 2 as the rate-limiting step and  $\text{O}_{\text{ads}}^- \cdots \text{MO}^+(\text{s})$  as the dominant species because of the fast dissociation of  $\text{N}_2\text{O}_{\text{ads}}^-$  (Fig. 12a).<sup>152</sup> Therefore, the  $\text{N}_2$  formation rate sharply increased and then saturated within the initial reaction stage over  $\text{ZnO}$ , in which case the kinetics was much faster than in the case of the photocatalytic reaction (Fig. 12b). Although the quantum efficiency of photo-assisted dissociation was small, an additional increase in  $\text{N}_2$  generation clearly appeared with time, and the reaction pathway (*i.e.*,  $\text{N}_2\text{O}_{\text{ads}} + (\text{e}^- + \text{h}^+) \rightarrow \text{N}_2\text{O}_{\text{ads}}^* \rightarrow \text{N}_2(\text{g}) + \text{O}_{\text{ads}}$ ) was specified by the migration of photogenerated charge carriers to the surface of  $\text{ZnO}$ . Electron paramagnetic resonance spectroscopy revealed that electrons are transferred to  $\text{N}_2\text{O}_{\text{ads}}$  ( $\text{N}_2\text{O}_{\text{ads}} + \text{e}^- \rightarrow \text{N}_2(\text{g}) + \text{O}_{\text{ads}}^-$ ), and  $\text{O}_{\text{ads}}^-$  might be localized at oxide ion vacancies via migration, while holes can be trapped at oxide ions via migration through the lattice.<sup>153</sup> Anpo *et al.* detected hyperfine splitting caused by one nitrogen atom at 77 K, which indicated the formation of either  $\text{N}_2\text{O}^-$  or  $\text{N}_2\text{O}_2^-$  ( $\text{N}_2\text{O} + \text{O}^- \rightarrow \text{N}_2\text{O}_2^-$ ) on  $\text{TiO}_2$  supported by porous Vycor glass.<sup>154,155</sup>

Kudo *et al.* reported the denitrification of  $\text{N}_2\text{O}$  over metal ( $\text{Pt}$ ,  $\text{Ag}$ , and  $\text{Cu}$ )-loaded  $\text{TiO}_2$  in the presence of electron donors (water or/and methanol vapor) under UV light.<sup>156,157</sup>  $\text{Pt}$  promoted the separation of electron–hole pairs, the dissociation of  $\text{N}_2\text{O}$ , and the supply of adsorbed hydrogen atoms (*i.e.*,  $\text{H}^+ + \text{e}^- \rightarrow \text{H}$ ;  $\text{N}_2\text{O} + 2\text{H} \rightarrow \text{N}_2 + \text{H}_2\text{O}$ ;  $\text{N}_2\text{O}^- + \text{H} \rightarrow \text{N}_2 + \text{OH}^-$ ), while water was oxidized on  $\text{TiO}_2$  ( $4\text{OH}^- + 4\text{h}^+ \rightarrow \text{O}_2 + 2\text{H}_2\text{O}$ ). In the presence of both water and  $\text{CH}_3\text{OH}$  vapor, the photocatalytic activity of  $\text{Pt}/\text{TiO}_2$  for  $\text{N}_2\text{O}$  reduction was almost negligible, as the photogenerated electrons were selectively transferred to

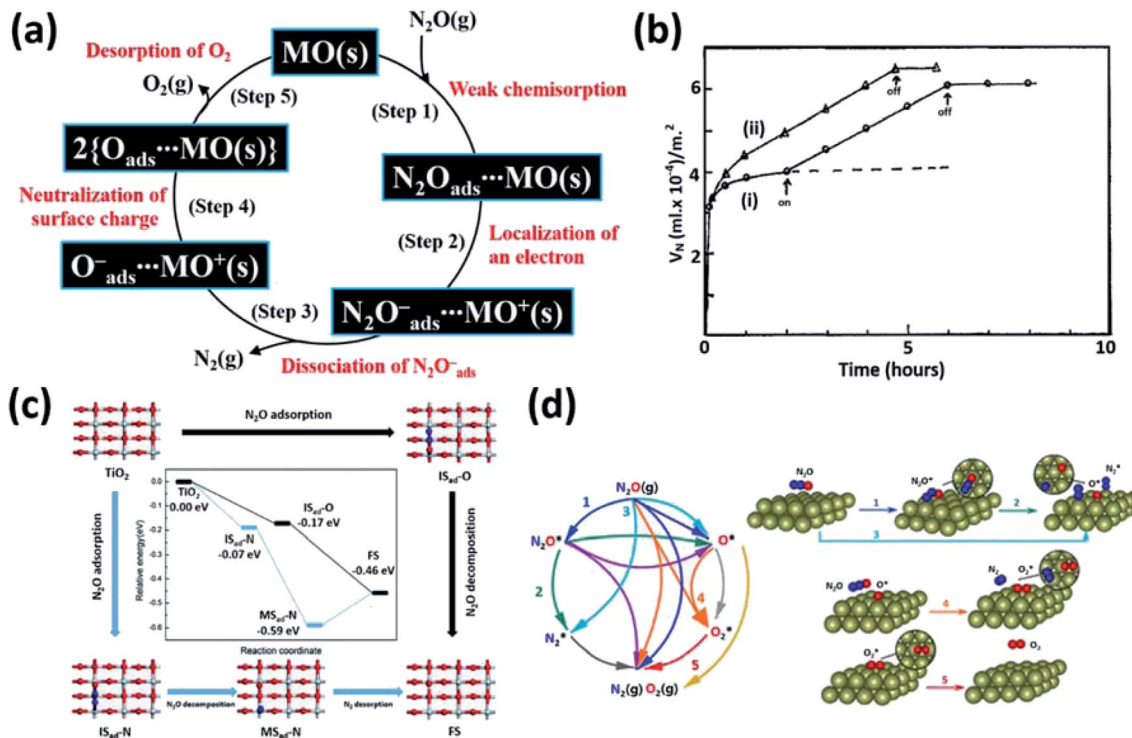


Fig. 12 (a) Mechanism of the conversion of  $\text{N}_2\text{O}$  to  $\text{N}_2$  and  $\text{O}_2$  over a metal oxide surface. (b) Time-dependent production of  $\text{N}_2$  ( $V_{\text{N}_2}$ ) from  $\text{N}_2\text{O}$  (10 Torr) over an activated ZnO surface at 20 °C under (i) dark and light on/off conditions indicated by arrows and (ii) continuous illumination. Reprinted with permission from ref. 152. Copyright© 1971, American Chemical Society. (c) Relative energy diagram for the photocatalytic decomposition of  $\text{N}_2\text{O}$  on perfect anatase (001) facets. Reprinted with permission from ref. 173. Copyright© 2018, Royal Society of Chemistry. (d) Reaction diagram for the conversion of  $\text{N}_2\text{O}$  to various adsorption and decomposition products ( $\text{N}_2\text{O}^*$ ,  $\text{N}_2^*$ ,  $\text{O}^*$ ,  $\text{O}_2^*$ ,  $\text{N}_2(\text{g})$  and  $\text{O}_2(\text{g})$ ); \* designates adsorbed species. (1–3) Dissociative adsorption of  $\text{N}_2\text{O}$  on Ir(111), (4) formation of surface peroxides, and (5)  $\text{O}_2$  desorption from Ir(111). Reprinted with permission from ref. 177. Copyright© 2019, American Chemical Society.

water to produce  $\text{H}_2$ . Ag- and Cu-loaded  $\text{TiO}_2$  promoted denitrification, probably because of the facile dissociation of  $\text{N}_2\text{O}_{\text{ads}}$  on Au and Cu surfaces as well as the relatively high kinetic barrier for the reduction of water by electrons. Sano *et al.* further probed the removal of  $\text{N}_2\text{O}$  over Ag/ $\text{TiO}_2$  in the presence of  $\text{CH}_3\text{OH}$  vapor and showed that the photocatalytic performance was affected by the oxidation state of Ag.<sup>158</sup> In particular, partially reduced  $\text{Ag}_2\text{O}$  prepared by photodeposition was more active than metallic Ag, which was ascribed to  $\text{Ag}^+$ -mediated charge transfer ( $\text{N}_2\text{O}_{\text{ads}} + \text{e}^- \rightarrow \text{N}_2\text{O}^-_{\text{ads}}$ ;  $\text{N}_2\text{O}^-_{\text{ads}} + \text{Ag}^+ \rightarrow \text{N}_2 + \text{Ag}-\text{O}$ ;  $3\text{Ag}-\text{O} + \text{CH}_3\text{OH}_{\text{ads}} + 3\text{h}^+ \rightarrow 3\text{Ag}^+ + \text{CO}_2 + 2\text{H}_2\text{O}$ ).

Metal ions ( $\text{Cu}^+$ ,  $\text{Ag}^+$ ,  $\text{Pb}^{2+}$ , and  $\text{Pr}^{3+}$ ) were immobilized on the surface of metal oxides ( $\text{SiO}_2$ ,  $\text{Al}_2\text{O}_3$ , and  $\text{SiO}_2/\text{Al}_2\text{O}_3$ ) or incorporated inside ZSM-5 zeolite pores to promote the photo-assisted removal of  $\text{N}_2\text{O}$ .  $\text{Cu}^+$ -anchored metal oxides were prepared by an ion-exchange method with thermovacuum treatment, and linear two-coordinate and planar three-coordinate  $\text{Cu}^+$  ions were observed on  $\text{SiO}_2/\text{Al}_2\text{O}_3$  and  $\text{Al}_2\text{O}_3$  or  $\text{SiO}_2$ , respectively.<sup>159</sup> In this case,  $\text{Cu}^+$  was assumed to undergo a  $(3\text{d}^{10})^1\text{S}_0 \rightarrow (3\text{d})^9(4\text{s})^1\text{D}_2$  electronic transition under UV light irradiation, and electron transfer from the photo-excited  $\text{Cu}^+$  to  $\text{N}_2\text{O}$  initiated denitrification. Photocatalytic activity was affected by the coordination geometry (linear or planar) and the aggregation state (isolated  $\text{Cu}^+$  monomer or  $\text{Cu}^+-\text{Cu}^+$  dimer) of  $\text{Cu}^+$  and was the highest for the isolated linearly coordinated

$\text{Cu}^+$  monomer owing to the long lifetime of charge carriers coupled with the low accumulation of  $\text{O}_{\text{ads}}$  due to  $\text{O}_2$  release. As  $\text{Cu}^+$  was incorporated in ZSM-5 and Y zeolite cavities, the type of  $\text{Cu}^+$  species depended on the degassing temperature, which suggested that the excited state of the  $\text{Cu}^+-\text{Cu}^+$  dimer was an effective  $\text{N}_2\text{O}$  quencher.<sup>160–162</sup> In the case of  $\text{Ag}^+$ -exchanged ZSM5, UV light irradiation induced the  $4\text{d}^{10} \rightarrow 4\text{d}^95\text{s}^1$  transition of two-coordinate isolated  $\text{Ag}^+$  ions, and the complexation of  $\text{Ag}^+$  with  $\text{N}_2\text{O}$  provided a channel for electron transfer from the excited  $\text{Ag}^+$  to the antibonding molecular orbital of  $\text{N}_2\text{O}$ .<sup>163</sup> For  $\text{Pb}^{2+}$ -exchanged and  $\text{Pr}^{3+}$ -supported catalysts, the reaction mechanisms were similar to those observed for  $\text{Cu}^+$ - and  $\text{Ag}^+$ -exchanged ones.<sup>164,165</sup>

Kočí's group reported diverse photocatalysts for the decomposition of  $\text{N}_2\text{O}$  under UV light irradiation, *e.g.*, ZnS/montmorillonite,<sup>166</sup> cordierite/steatite/ $\text{CeO}_2$ ,<sup>167</sup>  $\text{TiO}_2/\text{C}_3\text{N}_4$ ,<sup>168</sup>  $\text{WO}_3/\text{C}_3\text{N}_4$ ,<sup>169</sup>  $\text{ZnO}/\text{C}_3\text{N}_4$ ,<sup>170</sup>  $\text{BiOIO}_3/\text{C}_3\text{N}_4$ ,<sup>171</sup> and  $\text{BiVO}_4/\text{C}_3\text{N}_4$ .<sup>172</sup> Among them, binary photocatalyst combinations helped to inhibit charge carrier recombination and therefore exhibited enhanced photocatalytic denitrification performances. Although some of these photocatalysts exhibited visible-light activity, all experiments were carried out under UV light. Moreover, the physicochemical interactions between the catalyst surface and  $\text{N}_2\text{O}$  were not deeply investigated. To bridge this gap, Liu's group used DFT calculations to model the



decomposition of  $\text{N}_2\text{O}$  on  $\text{TiO}_2$ ,<sup>173</sup>  $\text{CeO}_2$ ,<sup>174</sup>  $\text{BiVO}_4$ ,<sup>175,176</sup>  $\text{BiMoO}_6$ ,<sup>176</sup> and  $\text{Bi}_2\text{WO}_6$ ,<sup>176</sup> obtaining results well correlated with experimental findings. For example, in the case of  $\text{TiO}_2$ , the photogenerated electrons did not affect  $\text{N}_2\text{O}$  adsorption, but the presence of oxygen vacancies or excited electrons promoted the  $\text{N}_2\text{O}$  decomposition reaction. The surface-trapped electrons at five-coordinate Ti ( $\text{Ti}_{5c}^{4+} + e^- \rightarrow \text{Ti}_{5c}^{3+}$ ) centers could act as active sites for N–O bond cleavage, with the reaction pathway depending on the adsorption geometry, *i.e.*, on whether  $\text{N}_2\text{O}$  ( $\text{O}=\text{N}^+=\text{N}^- \leftrightarrow ^-\text{O}-\text{N}^+\equiv\text{N}$ ) was adsorbed on  $\text{TiO}_2$  *via* the oxygen or the nitrogen end. In the case of decomposition on perfect anatase (001) facets, the  $\text{N}_2\text{O}$  adsorbed on  $\text{Ti}^{3+}$  *via* the oxygen end possessed an exothermic energy of 0.17 eV, and the O–N bond cleavage by the transfer of excited electrons from  $\text{Ti}^{3+}$  to  $\text{N}_2\text{O}$  featured an exothermicity of 0.29 eV and produced  $\text{N}_2$  (Fig. 12c). On the other hand, the  $\text{N}_2\text{O}$  adsorbed on  $\text{Ti}^{3+}$  *via* the nitrogen end formed an intermediate bridging configuration (with a binding energy of 0.19 eV), and the N–O bond cleavage was characterized by an enthalpy change of  $-0.40$  eV. Finally,  $\text{N}_2$  release from  $\text{TiO}_2$  was an endothermic (by 0.13 eV) process. The removal of  $\text{O}^-$  was ascribed to  $\text{O}^-$  discharge followed by recombination with another O atom, which proceeded *via* hole transfer to  $\text{O}^-$  and could decrease the energy barrier for  $\text{O}_2$  production.

An Al–Ir plasmonic antenna reactor combining plasmonic metallic antenna nanoparticles (Al nanocrystals) with nearby catalytic reactors (Ir nanoparticles) was designed for the photocatalytic conversion of  $\text{N}_2\text{O}$  to  $\text{N}_2$  and  $\text{O}_2$ .<sup>177</sup> At high GHSVs ( $\geq 80\,000\text{ h}^{-1}$ ), the conversion efficiency reached 10%, and  $\text{N}_2$  and  $\text{O}_2$  were the only products formed. The apparent activation energy was maintained irrespective of illumination, which suggested that photothermal heating rather than hot carriers generated by the plasmon effect was responsible for  $\text{N}_2\text{O}$  decomposition. As depicted in Fig. 12d, the pre-adsorption of  $\text{N}_2\text{O}$  on Ir (step 1) and the dissociation of  $\text{N}_2\text{O}$  (step 2) are not necessary because of the high exothermicity of the dissociative adsorption of  $\text{N}_2\text{O}(\text{g})$  into  $\text{N}_2^*$  and  $\text{O}^*$  at high operating temperatures (step 3). For fully saturated  $\text{O}^*$ , the direct interaction between  $\text{N}_2\text{O}(\text{g})$  and  $\text{O}^*$  can be driven by the Eley–Rideal mechanism to produce surface peroxide (step 4, moderately endothermic). Finally, the reaction is completed by the highly endothermic desorption of surface peroxide ( $\text{O}_2^*$ ; step 5), which was assumed to be the rate-limiting step for the overall  $\text{N}_2\text{O}$  decomposition on Ir(111).

### 3. Oxidation of ammonia to $\text{N}_2$ under aerobic and anaerobic conditions

Ammonia is one of the most valuable chemicals in agricultural and other industries, and has recently received much attention as a hydrogen carrier.<sup>178</sup> As the manufacture of  $\text{NH}_3$  by the Haber–Bosch process is highly energy-intensive and consumes  $\text{H}_2$  that is mainly derived from fossil fuels, the economically feasible utilization of  $\text{NH}_3$  as a hydrogen carrier requires the development of highly active catalysts for the production of  $\text{NH}_3$  and its decomposition to  $\text{H}_2$  under mild conditions.<sup>179,180</sup>

Therefore, much effort has been directed at the establishment of new methods of ambient-condition  $\text{N}_2$  fixation, particularly those using renewable energy resources.<sup>181</sup> Among these methods, the photocatalytic reduction of  $\text{N}_2$  to  $\text{NH}_3$  holds great promise, as the electrons and hydrogen are provided by sunlight and water, respectively, although the cleavage of the  $\text{N}\equiv\text{N}$  bond in  $\text{N}_2$  at standard temperature and pressure is a big challenge because of the low solubility of this gas.<sup>182</sup> From an environmental perspective,  $\text{NH}_3$  is not a useful chemical but a pollutant because of its high toxicity, corrosivity, odor, *etc.*, and should therefore be effectively removed from air and water. The expansion of agricultural infrastructure to satisfy the increasing global food demand is facilitating the release of  $\text{NH}_3$  (from fertilizers, livestock excretions, *etc.*) to the atmosphere and water bodies.<sup>183</sup> Most studies on photocatalysis target the oxidation of  $\text{NH}_3$  to  $\text{N}_2$  or  $\text{NO}_x$  ( $2\text{NH}_3 + 1.5\text{O}_2 \rightarrow \text{N}_2 + 3\text{H}_2\text{O}$ ,  $\Delta_r G_{298}^0 = -652.41\text{ kJ mol}^{-1}$ ;  $2\text{NH}_3 + 4\text{O}_2 \rightarrow 2\text{HNO}_3 + 2\text{H}_2\text{O}$ ,  $\Delta_r G_{298}^0 = -585.4\text{ kJ mol}^{-1}$ ), with comprehensive catalysts and relevant reaction mechanisms summarized in recent reviews.<sup>184,185</sup> Herein, we briefly describe the photocatalytic decomposition of  $\text{NH}_3$  on  $\text{TiO}_2$  and present several examples of relatively high performance for the selective conversion of  $\text{NH}_3$  to  $\text{N}_2$  at room temperature.

Fig. 13a presents the mechanism of the photocatalytic oxidation of gas-phase  $\text{NH}_3$  on  $\text{Pt}/\text{TiO}_2$  in the presence/absence of water vapor under anaerobic conditions.<sup>186</sup> Initially,  $\text{NH}_3$  is adsorbed on both Lewis- and Bronsted-acidic sites of  $\text{TiO}_2$  (mainly hydroxyl groups), and the reaction is initiated by the charge carriers generated under UV light irradiation. The electrons migrate to Pt nanoparticles to reduce protons and thus produce  $\text{H}_2$ . The oxidation of adsorbed  $\text{NH}_3$  occurs *via* hole transfer, and the coupling of two amide radicals ( $\text{NH}_2^{\cdot}$ ) produces  $\text{N}_2\text{H}_4$ , which can be subsequently converted into  $\text{H}_2$  and  $\text{N}_2\text{H}_2$ . Finally,  $\text{N}_2\text{H}_2$  self-decomposes into  $\text{N}_2$  and  $\text{H}_2$  or disproportionates into  $\text{N}_2$  and  $\text{N}_2\text{H}_4$ . As this process does not involve the formation of  $\text{NO}_x$ , the  $\text{H}_2:\text{N}_2$  molar ratio was recorded as 2.9, which was close to the theoretical value of 3.0 for the decomposition of  $\text{NH}_3$  to  $\text{N}_2$  and  $\text{H}_2$ . Although the hole-mediated oxidation of  $\text{NH}_2^{\cdot}$  to N through NH to release  $\text{N}_2$  is also possible, it is energetically unfavorable because of its higher net activation energy.<sup>160</sup> Under dry conditions, the accumulation of  $\text{NH}_4^+$  ions on  $\text{TiO}_2$  promotes catalyst deactivation, as these ions cannot easily migrate to Pt nanoparticles in the absence of water (Fig. 13b).

When  $\text{TiO}_2$  is used under aerobic and humid conditions, various nitrogen-containing species (*e.g.*,  $\text{NO}$ ,  $\text{NO}_2$ ,  $\text{NO}_2^-$ ,  $\text{NO}_3^-$ ,  $\text{N}_2\text{O}$ ,  $\text{HONO}$ , and  $\text{N}_2\text{H}_4$ ) might be involved as intermediates or produced as by-products during  $\text{NH}_3$  oxidation,<sup>188–194</sup> which complicates the selective production of  $\text{N}_2$ . When the experiment was carried out by irradiating  $\text{TiO}_2$  in a flow tube with a stream of  $\text{NH}_3$ -containing air,  $\text{HONO}$  was formed as an intermediate.<sup>190</sup> The production of  $\text{HONO}$  was negligible in the absence of  $\text{O}_2$  and exhibited a volcano-type dependence on the concentration of  $\text{NH}_3$ . The increase in  $[\text{HONO}]$  was ascribed to the photoreduction of  $\text{NO}_2$  ( $\text{NH}_3 \rightarrow \text{NO}_2 \rightarrow \text{HONO}$ ), while the decrease in  $[\text{HONO}]$  at higher  $\text{NH}_3$  concentrations was ascribed to the saturation of surface-active sites according to the



Fig. 13 Proposed mechanism of the photocatalytic decomposition of  $\text{NH}_3$  on Pt/TiO<sub>2</sub> in the (a) presence and (b) absence of water. Reprinted with permission from ref. 186. Copyright© 2012, American Chemical Society.

Langmuir–Hinshelwood model and the reaction with  $\text{NH}_3$  ( $\text{NH}_3 + \text{HONO} \rightarrow \text{NH}_4\text{NO}_2 \rightarrow \text{N}_2 + 2\text{H}_2\text{O}$ ). In a similar manner,  $[\text{HONO}]$  exhibited a volcano-like dependence on the relative humidity of the gas flow. Water accelerated the formation of HONO at low humidity, although excess water could occupy the pores of TiO<sub>2</sub>, hinder the access of  $\text{NH}_3$  to active sites, and facilitate the quenching of  $\text{OH}^{\cdot}$  to decrease  $[\text{HONO}]$ . In this experiment,  $\text{NO}_x$  was formed as the major by-product. Instead of probing the complete conversion of  $\text{NH}_3$  to  $\text{N}_2$ , almost all studies investigated the photocatalytic abatement of  $\text{NH}_3$  without analyzing the composition of the final products.

As mentioned earlier, the selective conversion of gaseous  $\text{NH}_3$  to  $\text{N}_2$  under aerobic conditions is challenging. From a practical viewpoint, operation under anaerobic conditions does not make sense, as the photocatalytic process is designed to remove few-ppm-level  $\text{NH}_3$  from air. In this regard, an anammox-like process aims to completely remove nitrogen species from aqueous systems (mainly  $\text{NH}_3$ -containing wastewater) or use concentrated  $\text{NH}_3$  solutions as hydrogen carriers to provide  $\text{H}_2$  for fuel cells and should be more feasible owing to

the ease of inert atmosphere generation *via*  $\text{N}_2$  or Ar purging. The protonation of  $\text{NH}_3$  ( $\text{pK}_a \approx 9.25$ ) and the positive change of TiO<sub>2</sub> surface charge ( $\text{pH}_{\text{zpc}} 6\text{--}7$  for P25) in acidic and neutral media cause electrostatic repulsion (*i.e.*,  $\text{NH}_4^+ \leftrightarrow >\text{Ti-OH}_2^+$ ), which hinders the adsorption of  $\text{NH}_4^+$  and inhibits the photocatalytic reaction.<sup>195</sup> Moreover, whereas  $\text{NH}_4^+$  is stable against attack by  $\text{OH}^{\cdot}$ , neutral  $\text{NH}_3$  is degraded by  $\text{OH}^{\cdot}$  under photocatalytic conditions.<sup>196–198</sup> Therefore, high photocatalytic performance was achieved at pH 10–11, whereas an activity decrease was observed at higher pH, probably because of the low solubility of  $\text{NH}_3$  under these conditions.

The use of metal nanoparticles as co-catalysts offers a simple way to increase the yield and selectivity of photocatalytic processes, prolong charge carrier lifetime, and provide catalytically active sites. Among the various metal nanoparticles used in conjunction with TiO<sub>2</sub>, Pt nanoparticles exhibited an outstanding performance for the decomposition of  $\text{NH}_3$  into  $\text{N}_2$  and  $\text{H}_2$  under both oxic and anoxic conditions.<sup>199–201</sup> Based on the calculated adsorption energies, Pt ( $-394 \text{ kJ mol}^{-1}$ ) has a moderate atomic nitrogen affinity for  $\text{N}_2$  formation among the

tested metals (*e.g.*, Ag ( $-156 \text{ kJ mol}^{-1}$ ), Au ( $-162 \text{ kJ mol}^{-1}$ ), Rh ( $-448 \text{ kJ mol}^{-1}$ ), Ru ( $-525 \text{ kJ mol}^{-1}$ )).<sup>202</sup> In comparison with bare  $\text{TiO}_2$ , which generated only nitrite and nitrate as end-products under air-saturated conditions, the loading of Pt (0.2 wt%) accelerated the reaction kinetics and promoted the evolution of  $\text{N}_2$  to reduce the total N content in the  $\text{NH}_3$  solution.<sup>170</sup> Interestingly, the presence of  $\text{O}_2$  had little influence on the kinetics over Pt/ $\text{TiO}_2$ , for which the efficiency of the  $\text{NH}_3$  to  $\text{N}_2$  conversion after 2 h irradiation equaled 65–70% in both air and  $\text{N}_2$ . Pt nanoparticles on  $\text{TiO}_2$  probably stabilized  $\text{NH}_x$  species generated as intermediates by  $\text{OH}^\cdot$ -mediated chain reactions. When  $\text{O}_2$  was replaced by  $\text{N}_2\text{O}$ , more OH radicals were formed through the reductive dissociation of  $\text{N}_2\text{O}$  on Pt to increase the efficiency of the  $\text{NH}_3$  to  $\text{N}_2$  conversion to 80%. The photocatalytic conversion of  $\text{NH}_3$  and the selectivity for  $\text{N}_2$  simultaneously increased with the increase in the loading of Pt on TNTs under oxic conditions. In particular, an ammonia conversion of 100% (for  $[\text{NH}_3]_i = 20 \text{ ppm}$ ) and a selectivity of 87.5% were achieved after 3 h irradiation for Pt/TNTs (25 wt% Pt).<sup>200</sup> Although the reductive dissociation of  $\text{NH}_3$  on Pt and the overoxidation of  $\text{NH}_3$  on TNTs might be responsible for the formation of  $\text{N}_2$  and  $\text{NO}_x$  ions, respectively, it is still unclear whether the reductive dissociation of  $\text{NH}_3$  is energetically favorable or not, and the function of nitrogen hydrogen radicals

on Pt as electron/hole recombination centers remains to be explored.

Under anaerobic conditions, the  $\text{H}_2 : \text{N}_2$  molar ratio achieved at alkaline pH using metallized photocatalysts (Pt/ $\text{TiO}_2$ , Pt/Fe-doped  $\text{TiO}_2$ , Ni/ $\text{TiO}_2$ ,  $\text{Pt}_{0.9}\text{Au}_{0.1}/\text{TiO}_2$ , and Ru/ $\text{ZnS}$ ) was close to the theoretical molar ratio (3 : 1). The main advantage of the anammox-like process is its ability to achieve both the complete removal of  $\text{NH}_3$  from wastewater and the recovery of  $\text{H}_2$  as a fuel for fuel cells at room temperature under sunlight. For example, in a highly concentrated solution (0.59 M),  $\text{NH}_3$  was decomposed at pH 10–12 over Pt/ $\text{TiO}_2$  (0.5 wt% Pt) to afford  $\text{H}_2$  and  $\text{N}_2$  in a 3 : 1 molar ratio, and the catalyst performance was governed by Pt loading, pH, photocatalyst type, and co-catalyst type. Despite the lack of supporting evidence, Pt was assumed to provide active sites for the reduction of protons to  $\text{H}_2$ , while the oxidation of  $\text{NH}_3$  occurred on  $\text{TiO}_2$ . When Pt/Fe-doped  $\text{TiO}_2$  (0.5 wt% Pt and 1.0 wt% Fe) was tested in 0.59 M  $\text{NH}_3$  under UV light irradiation, a 3 : 1 (mol/mol)  $\text{H}_2 : \text{N}_2$  ratio was recorded.<sup>203</sup> The higher  $\text{H}_2$  yield of Pt/Fe-doped  $\text{TiO}_2$  ( $27 \mu\text{mol mg}_{\text{cat}}^{-1}$ ) than that of Pt/ $\text{TiO}_2$  ( $18 \mu\text{mol mg}_{\text{cat}}^{-1}$ ) was due to the better absorption of visible light in the former case. Except for the case of Ni/ $\text{TiO}_2$ , the loading of non-noble-metals (V, Cr, Mn, Fe, Co, and Cu) on  $\text{TiO}_2$  slightly decreased the  $\text{H}_2$  yield, whereas the  $\text{H}_2 : \text{N}_2$  molar ratio of 3 : 1 was maintained (0.59 M  $\text{NH}_3$ ).<sup>188</sup> As seen in Fig. 14a, the amounts of

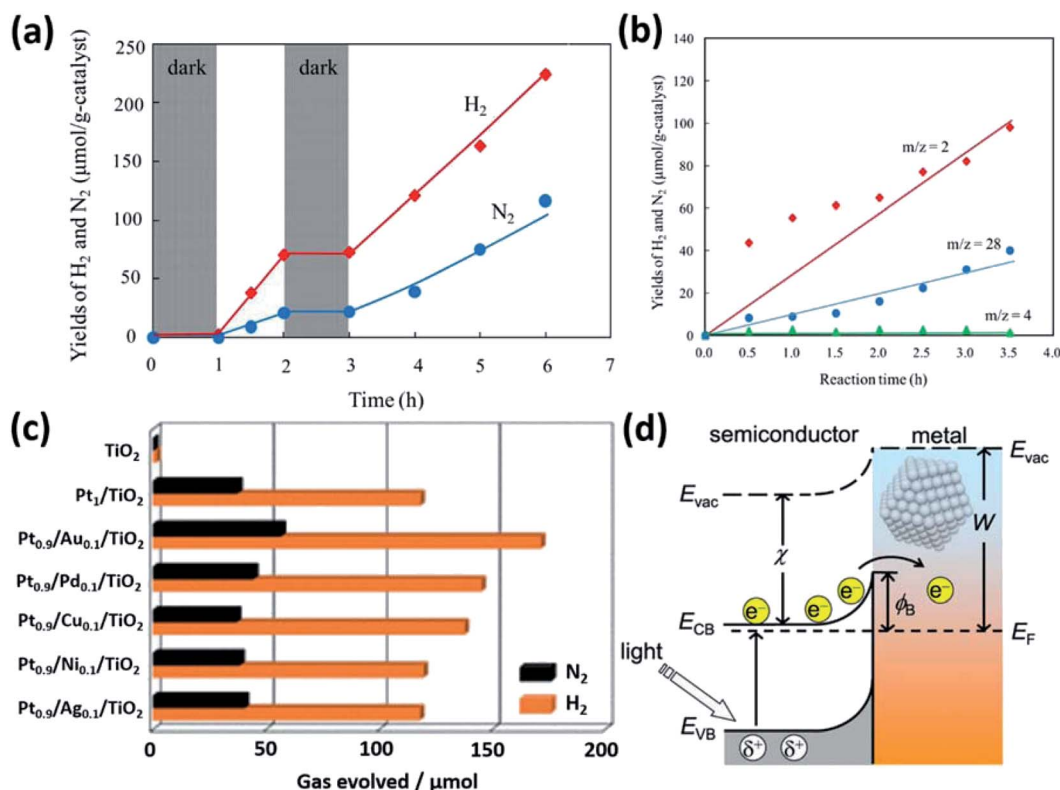


Fig. 14 (a) Time profiles of  $\text{H}_2$  and  $\text{N}_2$  production by the photodecomposition of  $\text{NH}_3$  over Ni/ $\text{TiO}_2$  (1.0 wt%) in the dark and under illumination. (b) Time profiles of gas-phase product yields for the photocatalytic decomposition of  $\text{NH}_3$  over Ni/ $\text{TiO}_2$  in  $\text{D}_2\text{O}$ . Reprinted with permission from ref. 187. Copyright© 2017, Elsevier. (c) Amounts of  $\text{H}_2$  and  $\text{N}_2$  evolved during the 6 h photocatalytic decomposition of  $\text{NH}_3$  on  $\text{Pt}_{0.9}\text{M}_{0.1}/\text{TiO}_2$  (M: Au, Pd, Cu, Ni, and Ag, total metal loading on  $\text{TiO}_2$ : 0.1 mol%). (d) Schematic electronic structure of a metal/semiconductor interface.  $E_{\text{vac}}$ ,  $E_{\text{F}}$ ,  $W$ ,  $\phi_{\text{B}}$ , and  $\chi$  denote the vacuum level, Fermi energy level, metal work function, Schottky barrier, and the electron affinity of the semiconductor conduction band, respectively. Reprinted with permission from ref. 204. Copyright© 2020, American Chemical Society.

$\text{N}_2$  and  $\text{H}_2$  produced over Ni/TiO<sub>2</sub> (0.5 wt% Ni) linearly increased with increasing irradiation time, and the reaction completely stopped in the dark. Isotope labeling experiments performed with D<sub>2</sub>O revealed that no D<sub>2</sub> and HD were produced, *i.e.*, the hydrogen in H<sub>2</sub> stemmed from NH<sub>3</sub> and not from water (Fig. 14b). This result indicates that the photodecomposition of NH<sub>3</sub> occurred on the interface between metal nanoparticles and TiO<sub>2</sub> and involved the direct migration of H<sup>•</sup> (formed by the hole-mediated reaction of NH<sub>3</sub>) to Pt. DFT calculations indicated the existence of two possible pathways for TiO<sub>2</sub>-based NH<sub>3</sub> decomposition, namely (i)  $2\text{NH}_3, \text{ads} \rightarrow 2\text{NH}_2^{\cdot} + \text{H}_2(\text{g}) \rightarrow \text{H}_2\text{N}-\text{NH}_2 + \text{H}_2(\text{g}) \rightarrow \cdot\text{N}=\text{N}^{\cdot} + 3\text{H}_2(\text{g}) \rightarrow \text{N}_2(\text{g}) + 3\text{H}_2(\text{g})$  and (ii)  $\text{NH}_3, \text{ads} + \text{NH}_3 \rightarrow \text{NH}_2^{\cdot} + \text{H}^{\cdot} + \text{NH}_3 \rightarrow \text{NH}_2-\text{NH}_3 + \text{H}^{\cdot} \rightarrow \text{H}_2\text{N}-\text{NH}_2 + \text{H}_2(\text{g}) \rightarrow \cdot\text{N}=\text{N}^{\cdot} + 3\text{H}_2(\text{g}) \rightarrow \text{N}_2(\text{g}) + 3\text{H}_2(\text{g})$ . The formation of NH<sub>2</sub>-NH<sub>2</sub> was probably assisted by metallic Ni. The loading of bimetallic alloy nanoparticles on TiO<sub>2</sub> is also a good way to enhance the photocatalytic activity of monometallic nanoparticle/TiO<sub>2</sub> hybrids, with the highest activity obtained for Pt<sub>0.9</sub>Au<sub>0.1</sub> under UV light irradiation (Fig. 14c).<sup>204</sup> As depicted in Fig. 14d, charge separation efficiency is determined by the Schottky barrier ( $\phi_{\text{B}}$ ;  $\phi_{\text{B}} = \text{metal work function } (W) - \text{electron affinity of the TiO}_2 \text{ conduction band } (\chi)$ ). The introduction of Au into Pt reduces  $\phi_{\text{B}}$ , which was calculated as 1.84, 1.62, and 0.97 eV for Pt/TiO<sub>2</sub>, Pt<sub>0.9</sub>Au<sub>0.1</sub>/TiO<sub>2</sub>, and Au/TiO<sub>2</sub>, respectively. Overly high and low  $\phi_{\text{B}}$  values suppress electron separation and promote reverse electron transfer, thus decelerating photocatalytic reactions. The decomposition of NH<sub>3</sub> into N<sub>2</sub> and H<sub>2</sub> was also carried out using other photocatalysts such as RuO<sub>2</sub>-NiO-SrTiO<sub>3</sub>,<sup>205</sup> ZnO,<sup>206</sup> and Ru/ZnS,<sup>207</sup> the activities of which were much lower than that of Pt/TiO<sub>2</sub>. The visible light-induced decomposition of NH<sub>3</sub> into N<sub>2</sub> and H<sub>2</sub> was also attempted in a dye-sensitized system comprising a homogeneous tris(bipyridine)ruthenium(II) (Ru(bpy)<sub>3</sub><sup>2+</sup>) dye, methyl viologen as an electron mediator, and O<sub>2</sub> as an electron acceptor.<sup>208</sup> Under visible light irradiation, Ru(bpy)<sub>3</sub><sup>3+</sup> oxidized NH<sub>3</sub> and was converted to the original state, Ru(bpy)<sub>3</sub><sup>2+</sup>.

## 4. Photoelectrochemical denitrification and ammonia oxidation

Only a few studies deal with photoelectrochemical denitrification and ammonia oxidation, focusing on the recovery of N<sub>2</sub> from nitrogen species. The photoelectrochemical denitrification of nitrite (1 mM NaNO<sub>2</sub> at pH 7) was first achieved in 1999 using a three-electrode system (counter electrode (CE) = Pt wire, reference electrode (RE) = saturated calomel electrode (SCE), and working electrode (WE) = roughened Ag electrode) in 0.1 M Na<sub>2</sub>SO<sub>4</sub> as an electrolyte under laser irradiation (362, 413, 457, 476, 488, 496, 514, and 647 nm) and a nitrogen atmosphere.<sup>209</sup> Denitrification was initiated by the excitation of Ag *via* plasmon resonance and the electrochemical current generated at -1.0 V<sub>SCE</sub>. Notably, irradiation brought about not only an increase in cathodic current but also a positive shift of the onset potential. The quantum efficiency was estimated as 0.04% without the analysis of real-time NO<sub>2</sub><sup>-</sup>, NO<sub>3</sub><sup>-</sup>, N<sub>2</sub>, and NH<sub>3</sub> concentrations. Nitrate reduction was believed to involve the electrochemical

nitrate to nitrite conversion followed by the photoelectrochemical reduction of nitrite to NH<sub>3</sub> and N<sub>2</sub>. The photoelectrochemical nitrate to nitrite conversion was also observed for Ag nanopyramids (1 M NaNO<sub>3</sub> at pH 5.7 under Ar), in which case the plasmon resonance of Ag resulted in an almost 100% faradaic efficiency at -1.0 V<sub>RHE</sub>.<sup>210</sup>

The photoelectrochemical nitrate to nitrite reduction was also promoted by semiconducting photocathode materials such as *p*-GaInP<sub>2</sub>, nanoporous *p*-Si, and CuI/PbI<sub>2</sub>. In the case of *p*-GaInP<sub>2</sub>, data were collected in a three-electrode system (CE = Pt black, RE = Ag/AgCl, and WE = *p*-GaInP<sub>2</sub>) in 0.1 M HNO<sub>3</sub> + 0.5 M NH<sub>4</sub>NO<sub>3</sub> as an electrolyte (pH 1) under simulated solar light at an air mass (AM) of 1.5 G.<sup>211</sup> The faradaic efficiency of nitrate reduction was calculated as 80%, and the incident-photon-to-current efficiency (IPCE) at -1.0 V<sub>Ag/AgCl</sub> was recorded as 100, 60, and 5% under excitation at 400, 580, and 610 nm, respectively. As a close to zero current was obtained in the dark, illumination was concluded to stimulate the rate-limiting step, and the catalytically active sites were assumed to be Ga and/or In. For nanoporous *p*-Si under similar conditions, the faradaic efficiency of nitrate reduction at -0.6 V<sub>Ag/AgCl</sub> equaled 65%, and no NH<sub>3</sub> and N<sub>2</sub> were observed.<sup>212</sup> In the case of CuI-PbI<sub>2</sub>, the faradaic efficiency of nitrate reduction in 0.1 M NaNO<sub>3</sub> exceeded 52%, and the IPCE at 400 nm was around 15%.<sup>213</sup> The bubbles evolved on the photoelectrode surface probably contained N<sub>2</sub> rather than H<sub>2</sub>, as no H<sub>2</sub> signal was observed by gas chromatography. Interestingly, isotope labeling experiments performed in Ar-saturated 0.1 M Na<sup>15</sup>NO<sub>3</sub> solution (98% <sup>15</sup>N) revealed that the generation of NH<sub>3</sub> was due to an external contamination and not nitrate reduction.

*n*-type semiconductors can be used as photoanodes for the water oxidation-induced conversion of nitrate to N<sub>2</sub>. In the presence of NH<sub>3</sub> as an electron donor (*i.e.*, using the same concept as that discussed in Section 2.2.1, the photo-SCR deNO<sub>x</sub>), ammonia oxidation and denitrification simultaneously occurred over TiO<sub>2</sub> and Pt black, respectively, in the absence of a bias voltage under UV light irradiation (1 mM NH<sub>3</sub>, 100 mM KNO<sub>3</sub>) (Fig. 15a).<sup>214</sup> When a mixture of pig urine/wash water (1/4) containing NH<sub>4</sub><sup>+</sup>, NO<sub>3</sub><sup>-</sup>, and NO<sub>2</sub><sup>-</sup> was tested under aerobic conditions, the following concentration decreases were observed after 24 h: NH<sub>4</sub><sup>+</sup> (2580 → 166 ppm), NO<sub>3</sub><sup>-</sup> (18.6 → 17.0 ppm), and NO<sub>2</sub><sup>-</sup> (4.84 → 3.17 ppm). The imbalance in the removal of NO<sub>x</sub><sup>-</sup> and NH<sub>4</sub><sup>+</sup> was ascribed to the competitive reduction of oxygen to H<sub>2</sub>O. Similarly, in a biophotochemical cell, H<sub>2</sub>O or biorefractory organics were oxidized at the photoanode, while denitrification proceeded at the biocathode.<sup>215,216</sup> The biocathode was prepared using activated sludge as an inoculum and was separated from the TiO<sub>2</sub> photoanode by a cation exchange membrane. As seen in Fig. 15b, the concentration of nitrate continuously decreased under illumination, whereas the abiotic cathode did not show any activity. Indeed, NO<sub>2</sub><sup>-</sup> and N<sub>2</sub>O were formed as intermediates, but the concentration of these intermediates and NO<sub>3</sub><sup>-</sup> decreased to zero after 30 h (Fig. 15c). NH<sub>4</sub><sup>+</sup> ions were always present at levels below the detection limit, which indicated that nitrate was selectively converted to N<sub>2</sub>. The faradaic efficiency of the cathode was

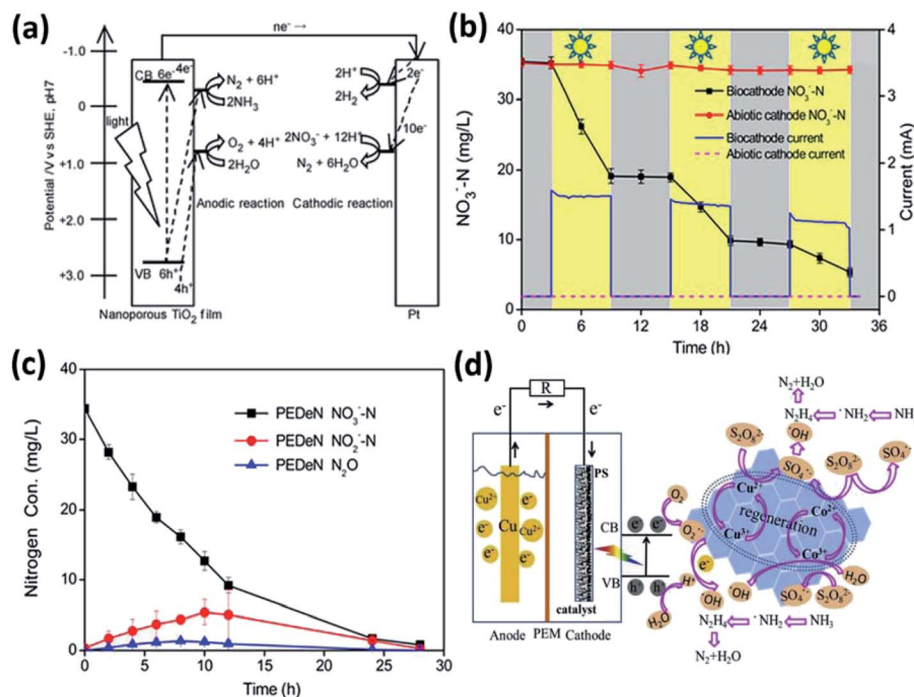


Fig. 15 (a) Photoelectrochemical denitrification of NO<sub>3</sub><sup>-</sup> to N<sub>2</sub> over a TiO<sub>2</sub> photoanode connected to a Pt cathode in the presence of NH<sub>3</sub> and H<sub>2</sub>O as electron donors under Ar. Reprinted with permission from ref. 214. Copyright© 2009, Royal Society of Chemistry. (b) Decrease of nitrate level under a photo-generated current during on–off intermittent illumination and (c) change of nitrogen oxide levels with time. Reprinted with permission from ref. 215. Copyright© 2017, American Chemical Society. (d) Proposed mechanism for the oxidation of NH<sub>3</sub> over a CuO/Co<sub>3</sub>O<sub>4</sub> photocathode in the presence of peroxydisulfate. Reprinted with permission from ref. 219. Copyright© 2020, Elsevier.

estimated as 97%, and a small number of electrons was assumed to be consumed by microbial growth.

The photoelectrochemical oxidation of ammonia to N<sub>2</sub> can be accomplished using the anodic or cathodic reaction to control photogenerated holes or radical species (hydroxyl or sulfate radicals) activated by electrons, respectively.<sup>217–220</sup> In the employed system (CE = Pt wire, RE = Ag/AgCl, and WE = TiO<sub>2</sub> photoanode in 10 M NH<sub>3</sub> + 0.1 M KNO<sub>3</sub> at pH 14.1), the H<sub>2</sub> : N<sub>2</sub> molar ratio equaled 3.08 under short-circuit conditions after 2 h irradiation.<sup>188</sup> The holes in TiO<sub>2</sub> oxidized NH<sub>3</sub> to N<sub>2</sub>, and the electrons transferred to Pt reduced water to H<sub>2</sub>. The OH<sup>-</sup> and SO<sub>4</sub><sup>•-</sup> species generated by the activation of peroxydisulfate (S<sub>2</sub>O<sub>8</sub><sup>2-</sup> + e<sup>-</sup> → SO<sub>4</sub><sup>•-</sup> + SO<sub>4</sub><sup>2-</sup> and SO<sub>4</sub><sup>•-</sup> + H<sub>2</sub>O → H<sup>+</sup> + OH<sup>-</sup> + SO<sub>4</sub><sup>2-</sup>) at the CuO/Co<sub>3</sub>O<sub>4</sub> photocathode oxidized NH<sub>3</sub> to N<sub>2</sub> (Fig. 15d).<sup>219</sup> The removal of 96.1% NH<sub>3</sub> (100 ppm) was achieved under visible light irradiation, and the reactive sites were identified as Co and Cu species.

## 5. Summary and outlook

There are various methods of decreasing the levels of reactive nitrogen compounds, which can include systematic crop rotation, optimization of the timing and amount of fertilizer input, the breeding or development of genetically engineered varieties of crops for increased nitrogen utilization efficiency, direct up-cycling of used nitrogen to microbial protein, and the development of artificial denitrification/ammonia oxidation processes powered by renewable energy. Among them, the solar-

powered photocatalytic and photoelectrochemical approaches are promising and future-oriented ways to treat aqueous and airborne NO<sub>x</sub>, N<sub>2</sub>O, and NH<sub>3</sub> because of their economically feasible and environmentally benign nature. However, the low efficiency and selectivity to N<sub>2</sub> and the scale-up problems are still a bottleneck for practical applications. Basically, the efficiency of artificial solar-powered denitrification/ammonia oxidation can be determined by (i) the absorbance of photocatalysts, (ii) the electronic structure of semiconducting materials, (iii) the recombination of charge carriers (*i.e.*, the lifetime of photogenerated electrons and holes), (iv) the control of surface properties to suppress undesired reactions such as ammonification and the re-oxidation of intermediates and products, and (v) the surroundings (*e.g.*, the presence/absence of oxygen, different types of electron donors, pH, humidity, *etc.*). Due to the different reaction pathways, the development of new photocatalysts and the systematic design of reactors have to be different depending on the treatment of aqueous and gas phase NO<sub>x</sub>, N<sub>2</sub>O, and NH<sub>3</sub>. In an aqueous system, the bimetallic nanoparticles loaded on TiO<sub>2</sub> (*e.g.*, Pd–Cu and Pt–Cu) showed a high performance of NO<sub>3</sub><sup>-</sup> conversion selective to N<sub>2</sub>, which gives a hint that the separation of the catalytic sites, the reduction of NO<sub>3</sub><sup>-</sup> to NO<sub>2</sub><sup>-</sup> and the further reduction of NO<sub>2</sub><sup>-</sup> to N<sub>2</sub>, is important to increase the selectivity. Precise control of the N : H ratio at surface active sites of catalysts including Lewis acid sites and defect sites is particularly required to suppress ammonification and thus selectively convert NO<sub>2</sub><sup>-</sup> to harmless N<sub>2</sub>. The reason why it is hard to reach a high conversion

efficiency of  $\text{NO}_3^-$  or  $\text{NO}_2^-$  as well as a high selectivity to  $\text{N}_2$  is due to the competitive charge transfer to  $\text{H}^+$ ,  $\text{O}_2$ , and  $\text{H}_2\text{O}$  and the re-oxidation of intermediates and by-products. In the case of the photocatalytic treatment of airborne  $\text{NO}_x$  and  $\text{N}_2\text{O}$  to  $\text{N}_2$ , it has been thoroughly investigated during the last three decades, offering the advantages of using water instead of the explosive  $\text{H}_2$  and toxic  $\text{NH}_3$ , operation at standard temperature and pressure, a net zero carbon emission in the case of operation under natural sunlight, and the availability of cheap and environmentally benign materials. Although various strategies such as structure and morphology control, co-catalyst loading, heteroatom doping, and hybridization with different types of materials have been developed to overcome the bottleneck of the conversion of  $\text{NO}_x$  and  $\text{N}_2\text{O}$  to  $\text{N}_2$ , the problems of insufficiently selective charge transfer, low solar light absorption, poor catalytic activity, need for noble metals as co-catalysts, and the lack of long-term durability need to be addressed to minimize the environmental impact of airborne  $\text{NO}_x$  and  $\text{N}_2\text{O}$ . In order to increase the possibility of commercialization, the addition of sacrificial hole scavengers should be necessary, where organic pollutants, particularly persistent organic pollutants (POPs), and ammonia (or carbon monoxide) are good candidates for wastewater and polluted air treatment, respectively, to compensate the operation cost.

Although ammonia is a very important feedstock, its high toxicity, corrosivity, and noxious odor make it a pollutant from the perspective of the environmental management of the nitrogen cycle. Given the large annual production of ammonia *via* the Haber–Bosch process and the low nitrogen use efficiency of ammonia-based fertilizers, ammonia should be effectively removed from air and water on a comparable scale. Recently, considering ammonia as a hydrogen carrier, the development of highly active catalysts for the decomposition of ammonia to  $\text{H}_2$  and  $\text{N}_2$  under mild conditions is highly desired. Although the conventional photocatalytic processes have focused on ammonia abatement, directing the production of nitrate instead of  $\text{N}_2$ , with a future-oriented point of view, the photocatalytic recovery of  $\text{H}_2$  from concentrated ammonia solution seems quite promising for fuel cell applications. The oxidation of adsorbed  $\text{NH}_3$  occurring *via* photogenerated holes does not involve the formation of  $\text{NO}_x$ , but the  $\text{H}_2$ : $\text{N}_2$  molar ratio becomes close to the theoretical value of 3:1 through the decomposition of  $\text{NH}_3$  to  $\text{N}_2$  and  $\text{H}_2$ , which is driven at standard temperature and pressure under illumination.

A photoelectrochemical cell can selectively control the reduction and oxidation reaction of nitrogen-containing species, in which the photogenerated electron–hole pairs are easily separated and consequently participate in the denitrification and anammox upon applying extra bias. To date, very few studies have been reported, in particular targeting the removal of toxic nitrite and ammonia from wastewater; however, the application should be more suitable for anammox in order to secure  $\text{H}_2$  from concentrated ammonia. Contrary to photocatalysis, it does not need to separate  $\text{N}_2$  and  $\text{H}_2$  because the oxidation and the reduction are proceeded in the anode and cathode, respectively, which is compartmented by a membrane. Indeed, the addition of an electrolyte is unnecessary in that the

pH of concentrated ammonia solution ( $>12$ ) is conductive enough to transport ions in the electrolyte. The in-depth investigation and successful development of photoelectrochemical ammonia oxidation systems will enable a counterpart of (photo)electrocatalytic nitrogen fixation, in other words the combination of the production and the utilization of ammonia as a hydrogen carrier.

It is time to take this issue seriously and think about it, and photocatalysis is the greenest way to restore the nitrogen cycle with a future-oriented technology. In order to go one step further to commercialization, the following can be considered: (i) the development of new materials to overcome the intrinsic problems of photocatalysts, (ii) the control of composition, morphology, and size of catalysts (*e.g.*, high entropy alloy, single atom catalyst, *etc.*), (iii) the systematic modification of photocatalysts including hybridization such as ternary and quaternary composites, co-doping, anchoring homogeneous sensitizers or promoters, selective surface passivation, *etc.*, (iv) the separation of catalytic sites by the control of the boundary between the catalysts and supporter or by a Janus structure, (v) the precise control of the micro-environment on the catalysts or electrodes, (vi) the finding of suitable POPs and greenhouse gases that cannot be removed by conventional treatment or typical AOPs, (vii) the design of a photo-reactor and its scale-up, (viii) the combination with other processes such as the pretreatment or final treatment through biological processes, and (ix) *in situ* analysis (*e.g.*, time-resolved surface enhanced infrared absorption/Raman spectroscopy) to unveil the real-time charge transfer and the formation of intermediates for the optimization of desired reactions.

## Author contributions

Cheolwoo Park: investigation, visualization, writing – original draft. Hyelim Kwak: investigation, visualization, writing – original draft. Gun-hee Moon: conceptualization, supervision, writing – original draft. Wooyul Kim: conceptualization, supervision, writing – review & editing.

## Conflicts of interest

There are no conflicts to declare.

## Acknowledgements

This research was financially supported by the Basic Science Research Program (NRF-2019R1C1C1006833) funded by the Korea government (MSIT) through the National Research Foundation of Korea (NRF), the Ecological Imitation-Based Environmental Pollution Management Technology Development Project funded by the Korea government (MOE) through KEITI (No. 2019002790008), the National Research Foundation of Korea (NRF) funded by the Ministry of Science and ICT (NRF-2020M3H4A3106354), and the KIST internal project (3E311191) funded by the Korea Institute of Science and Technology (KIST).

## Notes and references

- 1 A. Bernhard, *Nat. Educ. Knowl.*, 2010, **2**, 1–8.
- 2 D. E. Canfield, A. N. Glazer and P. G. Falkowski, *Science*, 2010, **330**, 192–196.
- 3 J. N. Galloway, A. M. Leach, A. Bleeker and J. W. Erisman, *Philos. Trans. R. Soc., B*, 2013, **368**, 20130120.
- 4 M. A. Sutton, C. M. Howard, T. K. Adhya, E. Baker, J. Baron, A. Basir, W. Brownlie, C. Cordovil, W. de Vries, V. Eory, R. Green, H. Harmens, K. W. Hicks, R. Jeffery, D. Kanter, L. Lassaletta, A. Leip, C. Masso, T. H. Misselbrook, E. Nemitz, S. P. Nissanka, O. Oenema, S. Patra, M. Pradhan, J. Ometto, R. Purvaja, N. Raghuram, R. Ramesh, N. Read, D. S. Reay, E. Rowe, A. SanzCobena, S. Sharma, K. R. Sharp, U. Skiba, J. U. Smith, I. van der Beck, M. Vieno, and H. J. M. van Grinsven, *Nitrogen - Grasping the Challenge. A Manifesto for Science-In-Action through the International Nitrogen Management System*. Summary Report, Ecology & Hydrology, Edinburgh, UK, 2019.
- 5 Food and Agriculture Organization, *FAO Statistical Databases*, 2006, Rome, available at <http://faostat.fao.org/default.aspx>.
- 6 International Energy Agency, *IEA Statistical Databases*, 2015, Paris, available at <http://iea.org/data-and-statistics>.
- 7 *Revised 1996 IPCC Guidelines for National Greenhouse Gas Inventories*, ed. J. T. Houghton, L. G. Meria Filho, K. Lim, I. Trennton, I. Mamaty, Y. Bonduki, D. J. Griggs and B. A. Callander, IPCC, OECD, IEA, 1996.
- 8 D. Laffoley and J. M. Baxter, *Ocean Deoxygenation: Everyone's Problem*, IUCN, Global Marine and Polar Programme, 2019.
- 9 N. Gruber and J. N. Galloway, *Nature*, 2008, **451**, 293–296.
- 10 S. Matassa, D. J. Batstone, T. Hülsen, J. Schnoor and W. Verstraete, *Environ. Sci. Technol.*, 2015, **49**, 5247–5254.
- 11 S. P. Seitzinger, C. Kroeze, A. F. Bouwman, N. Caraco, F. Dentener and R. V. Styles, *Estuaries*, 2002, **25**, 640–655.
- 12 M. B. Peoples, J. Brockwell, D. F. Herridge, I. J. Rochester, B. J. R. Alves, S. Urquiaga, R. M. Boddey, F. D. Dakora, S. Bhattarai, S. L. Maskey, C. Sampet, B. Rerkasem, D. F. Khan, H. Hauggaard-Nielsen and E. S. Jensen, *Symbiosis*, 2009, **48**, 1–17.
- 13 Y. Lan, J. Chen, H. Zhang, W.-X. Zhang and J. Yang, *J. Mater. Chem. A*, 2020, **8**, 15853–15863.
- 14 W. Hong, L. Su, J. Wang, M. Jiang, Y. Ma and J. Yang, *Chem. Commun.*, 2020, **56**, 14685–14688.
- 15 F. Ni, Y. Ma, J. Chen, W. Luo and J. Yanga, *Chin. Chem. Lett.*, 2021, **32**, 2073–2078.
- 16 L. Su, D. Han, G. Zhu, H. Xu, W. Luo, L. Wang, W. Jiang, A. Dong and J. Yang, *Nano Lett.*, 2019, **19**, 5423–5430.
- 17 H. Xu, J. Wu, W. Luo, Q. Li, W. Zhang and J. Yang, *Small*, 2020, **16**, 2001775.
- 18 D. R. Keeney, R. L. Chen and D. A. Graetz, *Nature*, 1971, **233**, 66–67.
- 19 A. Kapoor and T. Viraraghavan, *J. Environ. Eng.*, 1997, **123**, 371–380.
- 20 H. O. N. Tugaoen, S. Garcia-Segura, K. Hristovski and P. Westerhoff, *Sci. Total Environ.*, 2017, **599–600**, 1524–1551.
- 21 Z. Geng, Z. Chen, Z. Li, X. Qi, X. Yang, W. Fan, Y. Guo, L. Zhang and M. Huo, *Dalton Trans.*, 2018, **47**, 11104–11112.
- 22 H. Xu, Y. Li, M. Ding, W. Chen, K. Wang and C. Lu, *ACS Sustainable Chem. Eng.*, 2018, **6**, 7042–7051.
- 23 S. Roy, *J. Phys. Chem. C*, 2020, **124**, 28345–28358.
- 24 H. Zhang, Z. Liu, Y. Li, C. Zhang, Y. Wang, W. Zhang, L. Wang, L. Niu, P. Wang and C. Wang, *Appl. Surf. Sci.*, 2020, **503**, 144092.
- 25 J. E. Silveira, A. R. Ribeiro, J. Carbajo, G. Pliego, J. A. Zazo and J. A. Casas, *Water Res.*, 2021, **200**, 117250.
- 26 L. Wang, W. Fu, Y. Zhuge, J. Wang, F. Yao, W. Zhong and X. Ge, *Chemosphere*, 2021, **278**, 130298.
- 27 T. Caswell, M. W. Dlamini, P. J. Miedziak, S. Patisson, P. R. Davies, S. H. Taylor and G. J. Hutchings, *Catal. Sci. Technol.*, 2020, **10**, 2082–2091.
- 28 H. Kominami, K. Kitsui, Y. Ishiyama and K. Hashimoto, *RSC Adv.*, 2014, **4**, 51576–51579.
- 29 H. Gekko, K. Hashimoto and H. Kominami, *Phys. Chem. Chem. Phys.*, 2012, **14**, 7965–7970.
- 30 W. L. Silver, D. J. Herman and M. K. Firestone, *Ecology*, 2001, **82**, 2410–2416.
- 31 E. M. Sander, B. Viridis and S. Freguia, *RSC Adv.*, 2015, **5**, 86572–86577.
- 32 H. Hirakawa, M. Hashimoto, Y. Shiraishi and T. Hirai, *ACS Catal.*, 2017, **7**, 3713–3720.
- 33 H. Kominami, A. Furusho, S.-y. Murakami, H. Inoue, Y. Kera and B. Ohtani, *Catal. Lett.*, 2001, **76**, 31–34.
- 34 K. Akihiko, D. Kazunari, M. Ken-ichi and O. Takaharu, *Chem. Lett.*, 1987, **16**, 1019–1022.
- 35 M. Duca and M. T. M. Koper, *Energy Environ. Sci.*, 2012, **5**, 9726–9742.
- 36 Z. Hou, J. Chu, C. Liu, J. Wang, A. Li, T. Lin and C. P. François-Xavier, *Chem. Eng. J.*, 2021, **415**, 2082–2091.
- 37 S. Lee, S. Kim, C. Park, W. Kim, S. Ryu and W. Choi, *Energy Environ. Sci.*, 2021, DOI: 10.1039/D1EE01342D.
- 38 P. Li, Z. Jin, Z. Fanga and G. Yu, *Energy Environ. Sci.*, 2021, **14**, 3522–3531.
- 39 M. Shand and J. A. Anderson, *Catal. Sci. Technol.*, 2013, **3**, 879–899.
- 40 H.-i. Kim, K. Kim, S. Park, W. Kim, S. Kim and J. Kim, *Sep. Purif. Technol.*, 2019, **209**, 580–587.
- 41 L. Lei, W. Wang, C. Wang, H. Fan, A. K. Yadav, N. Hu, Q. Zhong and P. Müller-Buschbaum, *J. Mater. Chem. A*, 2020, **8**, 23812–23819.
- 42 Q. Liu, S. Wang, Q. Ren, T. Li, G. Tu, S. Zhong, Y. Zhao and S. Bai, *J. Mater. Chem. A*, 2021, **9**, 1552–1562.
- 43 X. Li, H. Jiang, C. Ma, Z. Zhu, X. Song, X. Li, H. Wang, P. Huo and X. Chen, *J. Mater. Chem. A*, 2020, **8**, 18707–18714.
- 44 S. Lee, S. Kim, C. Park, G.-h. Moon, H.-J. Son, J.-O. Baeg, W. Kim and W. Choi, *ACS Sustainable Chem. Eng.*, 2020, **8**, 3709–3717.

- 45 H. Lee, S. Jee, R. Kim, H.-T. Bui, B. Kim, J.-K. Kim, K. Park, W. Choi, W. Kim and K. Choi, *Energy Environ. Sci.*, 2020, **13**, 519–526.
- 46 E.-T. Yun, H.-Y. Yoo, W. Kim, H.-E. Kim, G. Kang, H. Lee, S. Lee, T. Park, C. Lee, J.-H. Kim and J. Lee, *Appl. Catal., B*, 2017, **203**, 475–484.
- 47 Y. Zhang, W. Hu, D. Wang, B. J. Reinhart and J. Huang, *J. Mater. Chem. A*, 2021, **9**, 6180–6187.
- 48 S. Weon, E. Choi, H. Kim, J. Kim, H.-J. Park, S.-m. Kim, W. Kim and W. Choi, *Environ. Sci. Technol.*, 2018, **52**, 9330–9340.
- 49 Q. Guo, F. Liang, Z. Sun, Y. Wang, X.-B. Li, S.-G. Xia, Z. C. Zhang, L. Huang and L.-Z. Wu, *J. Mater. Chem. A*, 2020, **8**, 22601–22606.
- 50 J. Sá, C. A. Agüera, S. Gross and J. A. Anderson, *Appl. Catal., B*, 2009, **85**, 192–200.
- 51 J. A. Anderson, *Catal. Today*, 2011, **175**, 316–321.
- 52 W. Gao, R. Jin, J. Chen, X. Guan, H. Zeng, F. Zhang and N. Guan, *Catal. Today*, 2004, **90**, 331–336.
- 53 S. Rengaraj and X. Z. Li, Enhanced photocatalytic reduction reaction over Bi<sup>3+</sup>-TiO<sub>2</sub> nanoparticles in presence of formic acid as a hole scavenger, *Chemosphere*, 2007, **66**, 930–9383.
- 54 D. D. B. Luiz, S. L. F. Andersen, C. Berger, H. J. José and R. D. F. P. M. Moreira, *J. Photochem. Photobiol. A*, 2012, **246**, 36–44.
- 55 J. R. Pan, C. Huang, W. Hsieh and B. Wu, *Sep. Purif. Technol.*, 2012, **84**, 52–55.
- 56 K. Kobwittaya and S. Sirivithayapakorn, *APCBEE Proc.*, 2014, **10**, 321–325.
- 57 S.-E. Bae, K. L. Stewart and A. A. Gewirth, *J. Am. Chem. Soc.*, 2007, **129**, 10171–10180.
- 58 I. Sanjuán, L. García-Cruz, J. Solla-Gullón, E. Expósito and V. Montiel, *Electrochim. Acta*, 2020, **340**, 135914.
- 59 S. Hamid, M. A. Kumar, J.-I. Han, H. Kim and W. Lee, *Green Chem.*, 2017, **19**, 853–866.
- 60 H. Shin, S. Jung, S. Bae, W. Lee and H. Kim, *Environ. Sci. Technol.*, 2014, **48**, 12768–12774.
- 61 T. Gu, W. Teng, N. Bai, Z. Chen, J. Fan, W.-x. Zhang and D. Zhao, *J. Mater. Chem. A*, 2020, **8**, 9545–9553.
- 62 S. Jung, S. Bae and W. Lee, *Environ. Sci. Technol.*, 2014, **48**, 9651–9658.
- 63 A. J. Calandra, C. Tamayo, J. Herrera and A. J. Arvia, *Electrochim. Acta*, 1972, **17**, 2035–2053.
- 64 L. Li, Z. Xu, F. Liu, Y. Shao, J. Wang, H. Wan and S. Zheng, *J. Photochem. Photobiol., A*, 2010, **212**, 113–121.
- 65 H. Kominami, T. Nakaseko, Y. Shimada, A. Furusho, H. Inoue, S.-y. Murakami, Y. Kera and B. Ohtani, *Chem. Commun.*, 2005, 2933–2935.
- 66 O. S. G. P. Soares, M. F. R. Pereira, J. J. M. Órfão, J. L. Faria and C. G. Silva, *Chem. Eng. J.*, 2014, **251**, 123–130.
- 67 Z. Hou, F. Chen, J. Wang, C. P. François-Xavier and T. Wintgens, *Appl. Catal., B*, 2018, **232**, 124–134.
- 68 J. A. Zazo, P. García-Muñoz, G. Pliego, J. E. Silveira, P. Jaffe and J. A. Casas, *Appl. Catal., B*, 2020, **273**, 118930.
- 69 H. Kato and A. Kudo, *Phys. Chem. Chem. Phys.*, 2002, **4**, 2833–2838.
- 70 L. Mohapatra and K. Parida, *J. Mater. Chem. A*, 2016, **4**, 10744–10766.
- 71 N. Dewangan, W. M. Hui, S. Jayaprakash, A.-R. Bawah, A. J. Poerjoto, T. Jie, A. Jangam, K. Hidajat, S. Kawi, *Catal. Today*, **356**, 490–513.
- 72 S. Zhang, Y. Zhao, R. Shi, C. Zhou, G. I. N. Waterhouse, L.-Z. Wu, C.-H. Tung and T. Zhang, *Adv. Energy Mater.*, 2020, **10**, 1901973.
- 73 D. P. Sahoo, K. K. Das, S. Patnaik and K. Parida, *Inorg. Chem. Front.*, 2020, **7**, 3695–3717.
- 74 Y. Zhao, G. Chen, T. Bian, C. Zhou, G. I. N. Waterhouse, L.-Z. Wu, C.-H. Tung, L. J. Smith, D. O'Hare and T. Zhang, *Adv. Mater.*, 2015, **27**, 7824–7831.
- 75 M. Adachi and A. Kudo, *Chem. Lett.*, 2012, **41**, 1007–1008.
- 76 X. Li, S. Wang, H. An, G. Dong, J. Feng, T. Wei, Y. Ren and J. Ma, *Appl. Surf. Sci.*, 2021, **539**, 148257.
- 77 M. Yue, R. Wang, B. Ma, R. Cong, W. Gao and T. Yang, *Catal. Sci. Technol.*, 2016, **6**, 8300–8308.
- 78 R. Wang, M. Yue, R. Cong, W. Gao and T. Yang, *J. Alloys Compd.*, 2015, **651**, 731–736.
- 79 B. Wang, B. An, Z. Su, L. Li and Y. Liu, *Chemosphere*, 2021, **269**, 128754.
- 80 G. Liu, S. You, M. Ma, H. Huang and N. Ren, *Environ. Sci. Technol.*, 2016, **50**, 11218–11225.
- 81 H.-T. Ren, S.-Y. Jia, J.-J. Zou, S.-H. Wu and X. Han, *Appl. Catal., B*, 2015, **176–177**, 53–61.
- 82 Y. Li and F. Wasgestian, *J. Photochem. Photobiol., A*, 1998, **112**, 255–259.
- 83 J. A. Anderson, *Catal. Today*, 2012, **181**, 171–176.
- 84 B. Bems, F. C. Jentoft and R. Schlögl, *Appl. Catal., B*, 1999, **20**, 155–163.
- 85 F. Zhang, Y. Pi, J. Cui, Y. Yang, X. Zhang and N. Guan, *J. Phys. Chem. C*, 2007, **111**, 3756–3761.
- 86 J. M. A. Freire, M. A. F. Matos, D. S. Abreu, H. Becker, I. C. N. Diógenes, A. Valentini and E. Longhinotti, *J. Environ. Chem. Eng.*, 2020, **8**, 103844.
- 87 A. Oita, A. Malik, K. Kanemoto, A. Geschke, S. Nishijima and M. Lenzen, *Nat. Geosci.*, 2016, **9**, 111–115.
- 88 D. S. Reay, E. A. Davidson, K. A. Smith, P. Smith, J. M. Melillo, F. Dentener and P. J. Crutzen, *Nat. Clim. Change*, 2012, **2**, 410–416.
- 89 G. Busca, L. Lietti, G. Ramis and F. Berti, *Appl. Catal., B*, 1998, **18**, 1–36.
- 90 L. Yang, A. Hakki, F. Wang and D. E. Macphee, *Appl. Catal., B*, 2018, **222**, 200–208.
- 91 Z. Gu, B. Zhang, Y. Asakura, S. Tsukuda, H. Kato, M. Kakihana and S. Yin, *Appl. Surf. Sci.*, 2020, **521**, 146213.
- 92 V. Khanal, N. O. Balayeva, C. Günnemann, Z. Mamiyev, R. Dillert, D. W. Bahnemann and V. R. Subramanian, *Appl. Catal., B*, 2021, **291**, 119974.
- 93 G. Liu, H. Xia, W. Zhang, L. Song, Q. Chen and Y. Niu, *J. Hazard. Mater.*, 2021, **418**, 126337.
- 94 J. V. C. d. Carmo, C. L. Lima, G. Mota, A. M. S. Santos, L. N. Costa, A. Ghosh, B. C. Viana, M. Silva, J. M. Soares, S. Tehuacanero-Cuapa, R. Lang, A. C. Oliveira, E. Rodríguez-Castellón and E. Rodríguez-Aguado, *Materials*, 2021, **14**, 2181.



- 95 W. Kim, T. Tachikawa, G.-h. Moon, T. Majima and W. Choi, *Angew. Chem., Int. Ed.*, 2014, **53**, 14036–14041.
- 96 Q. Wu and R. van de Krol, *J. Am. Chem. Soc.*, 2012, **134**, 9369–9375.
- 97 Q. Wu, Q. Zheng and R. van de Krol, *J. Phys. Chem. C*, 2012, **116**, 7219–7226.
- 98 G. Dong, D. L. Jacobs, L. Zang and C. Wang, *Appl. Catal., B*, 2017, **218**, 515–524.
- 99 M. Anpo, Y. Shioya, H. Yamashita, E. Giamello, C. Morterra, M. Che, H. H. Patterson, S. Webber and S. Ouellette, *J. Phys. Chem.*, 1994, **98**, 5744–5750.
- 100 M. Matsuoka, E. Matsuda, K. Tsuji, H. Yamashita and M. Anpo, *J. Mol. Catal. A: Chem.*, 1996, **107**, 399–403.
- 101 W.-S. Ju, M. Matsuoka and M. Anpo, *Catal. Lett.*, 2001, **71**, 91–93.
- 102 M. Anpo, S. G. Zhang, H. Mishima, M. Matsuoka and H. Yamashita, *Catal. Today*, 1997, **39**, 159–168.
- 103 Y. Hu, G. Martra, J. Zhang, S. Higashimoto, S. Coluccia and M. Anpo, *J. Phys. Chem. B*, 2006, **110**, 1680–1685.
- 104 M. Matsuoka and M. Anpo, in *Catalysis by Unique Metal Ion Structures in Solid Matrices*, ed. G. Centi, B. Wichterlová and A. T. Bell, Springer, Dordrecht, 2001, ch. Photocatalysis of Cations Incorporated within Zeolites, vol. 13, pp. 249–262.
- 105 M. Anpo, M. Matsuoka, K. Hanou, H. Mishima, H. Yamashita and H. H. Patterson, *Coord. Chem. Rev.*, 1998, **171**, 175–184.
- 106 M. Anpo and J. M. Thomas, *Chem. Commun.*, 2006, 3273–3278.
- 107 N. W. Cant and J. R. Cole, *J. Catal.*, 1992, **134**, 317–330.
- 108 T. Shishido, K. Teramura and T. Tanaka, *Catal. Sci. Technol.*, 2011, **1**, 541–551.
- 109 A. Yamamoto, K. Teramura and T. Tanaka, *Chem. Rec.*, 2016, **16**, 2268–2277.
- 110 K. Teramura, T. Tanaka and T. Funabiki, *Langmuir*, 2003, **19**, 1209–1214.
- 111 K. Teramura, T. Tanaka, S. Yamazoe, K. Arakaki and T. Funabiki, *Appl. Catal., B*, 2004, **53**, 29–36.
- 112 S. Yamazoe, T. Okumura, K. Teramura and T. Tanaka, *Catal. Today*, 2006, **111**, 266–270.
- 113 Y. Ji and Y. Luo, *J. Phys. Chem. C*, 2014, **118**, 6359–6364.
- 114 S. Yamazoe, Y. Masutani, T. Shishido and T. Tanaka, *Res. Chem. Intermed.*, 2008, **34**, 487–494.
- 115 S. Yamazoe, Y. Masutani, K. Teramura, Y. Hitomi, T. Shishido and T. Tanaka, *Appl. Catal., B*, 2008, **83**, 123–130.
- 116 R. Jin, Z. Wu, Y. Liu, B. Jiang and H. Wang, *J. Hazard. Mater.*, 2009, **161**, 42–48.
- 117 Y.-C. Chou and Y. Ku, *Chem. Eng. J.*, 2013, **225**, 734–743.
- 118 S. Yamazoe, K. Teramura, Y. Hitomi, T. Shishido and T. Tanaka, *J. Phys. Chem. C*, 2007, **111**, 14189–14197.
- 119 G. Zhang, G. Kim and W. Choi, *Energy Environ. Sci.*, 2014, **7**, 954–966.
- 120 A. Yamamoto, Y. Mizuno, K. Teramura, S. Hosokawa, T. Shishido and T. Tanaka, *Catal. Sci. Technol.*, 2015, **5**, 556–561.
- 121 A. Yamamoto, K. Teramura, S. Hosokawa, T. Shishido and T. Tanaka, *ChemCatChem*, 2015, **7**, 1818–1825.
- 122 X. Li, X. Yan, S. Zuo, X. Lu, S. Luo, Z. Li, C. Yao and C. Ni, *Chem. Eng. J.*, 2017, **320**, 211–221.
- 123 H. Zhang, X. Li, Y. Hui, L. Yu, Q. Xia, S. Luo and C. Yao, *J. Mater. Sci.: Mater. Electron.*, 2017, **28**, 9371–9377.
- 124 X. Li, H. Shi, W. Zhu, S. Zuo, X. Lu, S. Luo, Z. Li, C. Yao and Y. Chen, *Appl. Catal., B*, 2018, **231**, 92–100.
- 125 K. Wei, X. Yan, S. Zuo, W. Zhu, F. Wu, X. Li, C. Yao and X. Liu, *Clays Clay Miner.*, 2019, **67**, 348–356.
- 126 Z. Zhang, H. Lü, X. Li, X. Li, S. Ran, Z. Chen, Y. Yang, X. Wu and L. Li, *ACS Sustainable Chem. Eng.*, 2019, **7**, 10299–10309.
- 127 X. Li, H. Shi, X. Yan, S. Zuo, Y. Zhang, T. Wang, S. Luo, C. Yao and C. Ni, *ACS Sustainable Chem. Eng.*, 2018, **6**, 10616–10627.
- 128 X. Li, H. Shi, T. Wang, Y. Zhang, X. Lu, S. Zuo, Z. Li and C. Yao, *J. Taiwan Inst. Chem. Eng.*, 2018, **89**, 119–128.
- 129 X. Li, X. Yan, X. Lu, S. Zuo, Z. Li, C. Yao and C. Ni, *J. Catal.*, 2018, **357**, 59–68.
- 130 X. Li, H. Shi, X. Yan, S. Zuo, Y. Zhang, Q. Chen, C. Yao and C. Ni, *J. Catal.*, 2019, **369**, 190–200.
- 131 X. Li, Z. Wang, H. Shi, D. Dai, S. Zuo, C. Yao and C. Ni, *J. Hazard. Mater.*, 2020, **386**, 121977.
- 132 X. Li, H. Zhang, H. Lü, S. Zuo, Y. Zhang and C. Yao, *Environ. Sci. Pollut. Res.*, 2019, **26**, 12842–12850.
- 133 X. Li, Z. Wang, X. Chu, B. Gao, S. Zuo, W. Liu and C. Yao, *Appl. Clay Sci.*, 2020, **199**, 105871.
- 134 H. I. Hamoud, M. Lafjah, F. Douma, O. I. Lebedev, F. Djafri, V. Valchev, M. Daturi and M. El-Roz, *Sol. Energy*, 2019, **189**, 244–253.
- 135 N. Bowering, G. S. Walker and P. G. Harrison, *Appl. Catal., B*, 2006, **62**, 208–216.
- 136 N. Bowering, D. Croston, P. G. Harrison and G. S. Walker, *Int. J. Photoenergy*, 2007, **2007**, 090752.
- 137 A. A. Lisachenko, R. V. Mikhailov, L. L. Basov, B. N. Shelimov and M. Che, *J. Phys. Chem. C*, 2007, **111**, 14440–14447.
- 138 C. H. Ao, S. C. Lee, C. L. Mak and L. Y. Chan, *Appl. Catal., B*, 2003, **42**, 119–129.
- 139 S. Poulston, M. V. Twigg and A. P. Walker, *Appl. Catal., B*, 2009, **89**, 335–341.
- 140 Y.-T. Wu, Y.-H. Yu, V.-H. Nguyen and J. C. S. Wu, *Res. Chem. Intermed.*, 2015, **41**, 2153–2164.
- 141 Y.-H. Yu, I.-H. Su and J. C. S. Wu, *Environ. Technol.*, 2010, **31**, 1449–1458.
- 142 J. Lasek, Y.-H. Yu and J. C. S. Wu, *Environ. Technol.*, 2012, **33**, 2133–2141.
- 143 Y.-H. Yu, Y.-T. Pan, Y.-T. Wu, J. Lasek and J. C. S. Wu, *Catal. Today*, 2011, **174**, 141–147.
- 144 I. H. Su and J. C. S. Wu, *Catal. Commun.*, 2009, **10**, 1534–1537.
- 145 J. C.-C. Yu, V.-H. Nguyen, J. Lasek, S.-W. Chiang, D. X. Li and J. C. S. Wu, *Appl. Catal., A*, 2016, **523**, 294–303.
- 146 J. C.-C. Yu, V.-H. Nguyen, J. Lasek and J. C. S. Wu, *Appl. Catal., B*, 2017, **219**, 391–400.
- 147 J. C.-C. Yu, V.-H. Nguyen, J. Lasek, D. X. Li and J. C. S. Wu, *Catal. Commun.*, 2016, **84**, 40–43.

- 148 J. Miyawaki, T. Shimohara, N. Shirahama, A. Yasutake, M. Yoshikawa, I. Mochida and S.-H. Yoon, *Appl. Catal., B*, 2011, **110**, 273–278.
- 149 G. Halasi, T. Bánsági and F. Solymosi, *J. Catal.*, 2015, **325**, 60–67.
- 150 L. Liao, S. Heylen, S. P. Sree, B. Vallaey, M. Keulemans, S. Lenaerts, M. B. J. Roeffaers and J. A. Martens, *Appl. Catal., B*, 2017, **202**, 381–387.
- 151 G. Blyholder and K. Tanaka, *J. Phys. Chem.*, 1971, **75**, 1037–1043.
- 152 J. Cunningham, J. J. Kelly and A. L. Penny, *J. Phys. Chem.*, 1971, **75**, 617–625.
- 153 N. B. Wong, Y. B. Taarit and J. H. Lunsford, *J. Chem. Phys.*, 1974, **60**, 2148–2151.
- 154 M. Anpo, N. Aikawa and Y. Kubokawa, *J. Chem. Soc., Chem. Commun.*, 1984, 644–645.
- 155 M. Anpo, N. Aikawa, Y. Kubokawa, M. Che, C. Louis and E. Giamello, *J. Phys. Chem.*, 1985, **89**, 5689–5694.
- 156 A. Kudo and T. Sakata, *Chem. Lett.*, 1992, **21**, 2381–2384.
- 157 A. Kudo and H. Nagayoshi, *Catal. Lett.*, 1998, **52**, 109–111.
- 158 T. Sano, N. Negishi, D. Mas and K. Takeuchi, *J. Catal.*, 2000, **194**, 71–79.
- 159 M. Matsuoka, W.-S. Ju, K. Takahashi, H. Yamashita and M. Anpo, *J. Phys. Chem. B*, 2000, **104**, 4911–4915.
- 160 K. Ebitani, M. Morokuma, J.-H. Kim and A. Morikawa, *J. Catal.*, 1993, **141**, 725–728.
- 161 K. Ebitani, M. Morokuma, J.-H. Kim and A. Morikawa, *J. Chem. Soc., Faraday Trans.*, 1994, **90**, 377–381.
- 162 K. Ebitani, M. Morokuma and A. Morikawa, in *Stud. Surf. Sci. Catal.*, ed. J. Weitkamp, H. G. Karge, H. Pfeifer and W. Hölderich, Elsevier, 1994, vol. 84, pp. 1501–1506.
- 163 W.-S. Ju, M. Matsuoka, K. Iino, H. Yamashita and M. Anpo, *J. Phys. Chem. B*, 2004, **108**, 2128–2133.
- 164 W.-S. Ju, M. Matsuoka, H. Yamashita and M. Anpo, *J. Synchrotron Radiat.*, 2001, **8**, 608–609.
- 165 K. Ebitani, Y. Hirano and A. Morikawa, *J. Catal.*, 1995, **157**, 262–265.
- 166 L. Obalová, M. Šihor, P. Praus, M. Reli and K. Kočí, *Catal. Today*, 2014, **230**, 61–66.
- 167 M. Valášková, K. Kočí and J. Kupková, *Microporous Mesoporous Mater.*, 2015, **207**, 120–125.
- 168 K. Kočí, M. Reli, I. Troppová, M. Šihor, J. Kupková, P. Kustrowski and P. Praus, *Appl. Surf. Sci.*, 2017, **396**, 1685–1695.
- 169 M. Reli, L. Svoboda, M. Šihor, I. Troppová, J. Pavlovský, P. Praus and K. Kočí, *Environ. Sci. Pollut. Res. Int.*, 2018, **25**, 34839–34850.
- 170 K. Kočí, M. Reli, I. Troppová, M. Šihor, T. Bajcarová, M. Ritz, J. Pavlovský and P. Praus, *Catalysts*, 2019, **9**, 735.
- 171 V. Matějka, M. Šihor, M. Reli, A. Martaus, K. Kočí, M. Kormunda and P. Praus, *Mater. Sci. Semicond. Process.*, 2019, **100**, 113–122.
- 172 P. Praus, J. Lang, A. Martaus, L. Svoboda, V. Matějka, M. Kormunda, M. Šihor, M. Reli and K. Kočí, *J. Inorg. Organomet. Polym.*, 2019, **29**, 1219–1234.
- 173 L. Wang, W. Song, J. Deng, H. Zheng, J. Liu, Z. Zhao, M. Gao and Y. Wei, *Nanoscale*, 2018, **10**, 6024–6038.
- 174 W. Song, L. Wang, Y. Gao, J. Deng, M. Jing, H. Zheng, J. Liu, Z. Zhao, M. Gao and Y. Wei, *J. Mater. Chem. A*, 2018, **6**, 19241–19255.
- 175 L. Wang, J. Liu, W. Song, H. Wang, Y. Li, J. Liu, Z. Zhao, J. Tan, Z. Duan and J. Deng, *Chem. Eng. J.*, 2019, **366**, 504–513.
- 176 J. Liu, L. Wang, W. Song, M. Zhao, J. Liu, H. Wang, Z. Zhao, C. Xu and Z. Duan, *ACS Sustainable Chem. Eng.*, 2019, **7**, 2811–2820.
- 177 D. F. Swearer, H. Robotjazi, J. M. P. Martirez, M. Zhang, L. Zhou, E. A. Carter, P. Nordlander and N. J. Halas, *ACS Nano*, 2019, **13**, 8076–8086.
- 178 A. Klerke, C. H. Christensen, J. K. Nørskov and T. Vegge, *J. Mater. Chem.*, 2008, **18**, 2304–2310.
- 179 Q. Wang, J. Guo and P. Chen, *J. Energy Chem.*, 2019, **36**, 25–36.
- 180 F. Schüth, R. Palkovits, R. Schlögl and D. S. Su, *Energy Environ. Sci.*, 2012, **5**, 6278–6289.
- 181 X. Cui, C. Tang and Q. Zhang, *Adv. Energy Mater.*, 2018, **8**, 1800369.
- 182 Q. Han, H. Jiao, L. Xiong and J. Tang, *Adv. Mater.*, 2021, **2**, 564–581.
- 183 E. Stokstad, *Science*, 2014, **343**, 238.
- 184 K. Vikrant, K.-H. Kim, F. Dong and D. A. Giannakoudakis, *ACS Catal.*, 2020, **10**, 8683–8716.
- 185 S. Zhang, Z. He, X. Li, J. Zhang, Q. Zang and S. Wang, *Nanoscale Adv.*, 2020, **2**, 3610–3623.
- 186 H. Yuzawa, T. Mori, H. Itoh and H. Yoshida, *J. Phys. Chem. C*, 2012, **116**, 4126–4136.
- 187 A. Utsunomiya, A. Okemoto, Y. Nishino, K. Kitagawa, H. Kobayashi, K. Taniya, Y. Ichihashi and S. Nishiyama, *Appl. Catal., B*, 2017, **206**, 378–383.
- 188 A. C. Sola, D. Garzón Sousa, J. Araña, O. González Díaz, J. M. Doña Rodríguez, P. Ramírez de la Piscina and N. Homs, *Catal. Today*, 2016, **266**, 53–61.
- 189 H. Mozzanega, J. M. Herrmann and P. Pichat, *J. Phys. Chem.*, 1979, **83**, 2251–2255.
- 190 M. A. Kebede, N. K. Scharko, L. E. Appelt and J. D. Raff, *J. Phys. Chem. Lett.*, 2013, **4**, 2618–2623.
- 191 B. Boulinguez, A. Bouzaza, S. Merabet and D. Wolbert, *J. Photochem. Photobiol., A*, 2008, **200**, 254–261.
- 192 M. Chen, J. Ma, B. Zhang, F. Wang, Y. Li, C. Zhang and H. He, *Appl. Catal., B*, 2018, **223**, 209–215.
- 193 G. Zhang, J. Ruan and T. Du, *ACS ES&T Eng.*, 2021, **1**, 310–325.
- 194 J. Feng, X. Zhang, G. Zhang, J. Li, W. Song and Z. Xu, *Chemosphere*, 2021, **274**, 129689.
- 195 X. Zhu, S. R. Castleberry, M. A. Nanny and E. C. Butler, *Environ. Sci. Technol.*, 2005, **39**, 3784–3791.
- 196 R. Zellner and I. W. M. Smith, *Chem. Phys. Lett.*, 1974, **26**, 72–74.
- 197 E.-M. Bensen, S. Schroeter, H. Jacobs and J. C. Broekaert, *Chemosphere*, 1997, **35**, 1431–1445.
- 198 S. Kim and W. Choi, *Environ. Sci. Technol.*, 2002, **36**, 2019–2025.
- 199 J. Lee, H. Park and W. Choi, *Environ. Sci. Technol.*, 2002, **36**, 5462–5468.

- 200 H.-H. Ou, M. R. Hoffmann, C.-H. Liao, J.-H. Hong and S.-L. Lo, *Appl. Catal., B*, 2010, **99**, 74–80.
- 201 H. Kominami, H. Nishimune, Y. Ohta, Y. Arakawa and T. Inaba, *Appl. Catal., B*, 2012, **111–112**, 297–302.
- 202 A. C. A. de Vooy, M. T. M. Koper, R. A. van Santen and J. A. R. van Veen, *J. Electroanal. Chem.*, 2001, **506**, 127–137.
- 203 J. Nemoto, N. Gokan, H. Ueno and M. Kaneko, *J. Photochem. Photobiol., A*, 2007, **185**, 295–300.
- 204 Y. Shiraishi, S. Toi, S. Ichikawa and T. Hirai, *ACS Appl. Nano Mater.*, 2020, **3**, 1612–1620.
- 205 L. Qing-shui, D. Kazunari, N. Shuichi, O. Takaharu and T. Kenzi, *Chem. Lett.*, 1983, **12**, 321–324.
- 206 M. Reli, M. Edelmannová, M. Šíhor, P. Praus, L. Svoboda, K. K. Mamulová, H. Otoupalíková, L. Čapek, A. Hospodková, L. Obalová and K. Kočí, *Int. J. Hydrogen Energy*, 2015, **40**, 8530–8538.
- 207 A. Iwase, K. Ii and A. Kudo, *Chem. Commun.*, 2018, **54**, 6117–6119.
- 208 M. Kaneko, N. Katakura, C. Harada, Y. Takei and M. Hoshino, *Chem. Commun.*, 2005, 3436–3438.
- 209 J. Zheng, T. Lu, T. M. Cotton and G. Chumanov, *J. Phys. Chem. B*, 1999, **103**, 6567–6572.
- 210 Y. Kim, E. B. Creel, E. R. Corson, B. D. McCloskey, J. J. Urban and R. Kostecki, *Adv. Energy Mater.*, 2018, **8**, 1800363.
- 211 H. Wang and J. A. Turner, *Energy Environ. Sci.*, 2013, **6**, 1802–1805.
- 212 M. Kan, D. Yue, J. Jia and Y. Zhao, *Electrochim. Acta*, 2015, **177**, 366–369.
- 213 E. Kecsenovity, S. T. Kochuveedu, J.-P. Chou, D. Lukács, Á. Gali and C. Janáky, *Sol. RRL*, 2021, **5**, 2000418.
- 214 R. Saito, H. Ueno, J. Nemoto, Y. Fujii, A. Izuoka and M. Kaneko, *Chem. Commun.*, 2009, 3231–3233.
- 215 H.-Y. Cheng, X.-D. Tian, C.-H. Li, S.-S. Wang, S.-G. Su, H.-C. Wang, B. Zhang, H. M. A. Sharif and A.-J. Wang, *Environ. Sci. Technol.*, 2017, **51**, 12948–12955.
- 216 S. Su, Y. Zhang, W. Hu, X. Zhang, D. Ju, C. Jia and J. Liu, *Bioelectrochemistry*, 2020, **132**, 107439.
- 217 M. Kaneko, N. Gokan, N. Katakura, Y. Takei and M. Hoshino, *Chem. Commun.*, 2005, 1625–1627.
- 218 X. Fan, Y. Zhou, G. Zhang, T. Liu and W. Dong, *Appl. Catal., B*, 2019, **244**, 396–406.
- 219 C. Yan and L. Liu, *J. Hazard. Mater.*, 2020, **388**, 121793.
- 220 Y. Qu, X. Song, X. Chen, X. Fan and G. Zhang, *Chem. Eng. J.*, 2020, **382**, 123048.